System openness governs detectable signals of enhanced rock weathering in soils: a global meta-analysis

Zhaofeng Ouyang[a,b,1], Meitong Song[a,c,1], Xiaodan Tang[c], Yuyan Zhao[c], Simon A. T. Redfern[a,b,d,*]

[a] Asian School of the Environment, Nanyang Technological University, 50 Nanyang Avenue, Singapore 639798

[b] Earth Observatory of Singapore, Nanyang Technological University, 50 Nanyang Avenue, Singapore 639798

[c] College of Geoexploration Science and Technology, Jilin University, Changchun 130026, China

[d] School of Materials Science and Engineering, Nanyang Technological University, 50 Nanyang Avenue, Singapore 639748

* Corresponding author: simon.redfern@ntu.edu.sg

[1] These authors contributed equally to this work.

Preprint notice. This manuscript is a preprint deposited on EarthArXiv. It has been submitted for publication in *Global Change Biology* and has been revised in response to peer review; it has not been accepted for publication. Subsequent versions of this manuscript may differ in content. If accepted, the final version will be accessible via the Peer-reviewed Publication DOI link on the EarthArXiv record. The authors welcome feedback, which may be sent to the corresponding author.

Contents. Main text (29 pages) followed by the Supplementary Information (15 pages).

Data availability. The source data for this meta-analysis are available on FigShare at https://doi.org/10.6084/m9.figshare.31868998.

System openness governs detectable signals of enhanced rock weathering in soils: a global meta-analysis

Zhaofeng Ouyang[a,b 1], Meitong Song[a,c 1], Xiaodan Tang[c], Yuyan Zhao[c], Simon A. T. Redfern [a,b,d *]

[a] *Asian School of the Environment, Nanyang Technological University, 50 Nanyang Avenue, Singapore 639798.*

[b] *Earth Observatory of Singapore (EOS), Nanyang Technological University, 50 Nanyang Avenue, Singapore 639798.*

[c] *College of Geoexploration Science and Technology, Jilin University, Changchun 130026, China*

[d] *School of Materials Science and Engineering, Nanyang Technological University, 50 Nanyang Avenue, Singapore 639748.*

* Corresponding author. E-mail address: simon.redfern@ntu.edu.sg

[1] Zhaofeng Ouyang and Meitong Song contributed equally to this work.

Abstract

Substantial heterogeneity in enhanced rock weathering (ERW) outcomes is often attributed to dissolution controls. However, we show that experimental boundary conditions – especially system openness – provide a primary explanation because dissolution products can be redistributed or exported beyond the sampled pool. We synthesise 81 peer-reviewed ERW studies (205 comparisons) using treatment-driven changes in exchangeable Ca and Mg as indicators of retained near-field weathering products. These retained exchangeable signals attenuated from incubations to pots/mesocosms and field trials, indicating constraints from hydrological connectivity and sampling boundary. Meta-regression reveals application rate is the principal controllable lever, whereas particle-size effects in controlled studies are not independently robust once correlated design choices are accounted for. Baseline soil pH is a consistent contextual filter, while hydroclimate sensitivities inferred from controlled systems are not reliably expressed in field datasets. A mass-balance conversion anchored to the 0–20 cm exchangeable pool yielded small apparent retained CO_2-equivalent signals (~0.03–0.06 t

CO_2 ha^{-1} yr^{-1}), best interpreted as near-field retention constraints rather than standalone CDR estimates. We propose a boundary-aware framework matching exchangeable signals to system openness and accounting scope before tuning application rate. Robust attribution requires longer field trials pairing exchangeable pools with deeper soil, export and water chemistry.

Keywords:

Enhanced rock weathering; carbon dioxide removal; meta-analysis; exchangeable cations; system openness; weathering-product export

1 Introduction

Carbon dioxide removal (CDR) is increasingly recognised as a necessary complement to deep emissions reductions for mitigating climate warming (Goren et al., 2024). Enhanced rock weathering (ERW) has emerged as a promising CDR technology, with the potential to be deployed through existing agricultural supply chains by applying finely ground silicate rocks to cropland soils (Hartmann et al., 2013; Haque et al., 2019, 2023; Beerling et al., 2020). In principle, accelerated silicate dissolution consumes atmospheric CO_2 while releasing base cations and alkalinity that can ultimately be transported to the ocean and stored as dissolved inorganic carbon. Field trials of ERW are therefore expanding rapidly. However, reported outcomes vary widely across studies, and estimates of carbon removal derived from experimental evidence remain difficult to compare or reconcile.

A central but under-recognised reason for this variability is that most ERW experiments measure weathering signals within incomplete or non-equivalent system boundaries. Dissolution products generated in soil can be retained in near-field exchangeable pools, redistributed below the sampled layer, incorporated into plants or secondary phases, or exported hydrologically, meaning that the strength of a detectable signal depends not only on dissolution kinetics but also on the openness of the experimental system and the compartment sampled (White & Brantley, 2003). This boundary dependence is directly relevant to CDR attribution: exchangeable Ca and Mg measured in the sampled near-field soil pool record retained weathering products, but do not by themselves quantify exported alkalinity, whole-system carbon removal or durable CDR. The same boundary dependence also means that experiments conducted under different degrees of hydrological connectivity may report systematically different signals even when underlying silicate dissolution proceeds at comparable rates.

Here we test this hypothesis using a global meta-analysis of ERW experiments in soils. By synthesising 81 studies reporting treatment-driven changes in exchangeable Ca and Mg, we evaluate how experimental openness influences the detectability and interpretation of retained near-field exchangeable signals and how these signals interact with controllable design choices such as application rate and particle size**.** We show that much of this heterogeneity arises from differences in experimental boundary conditions rather than dissolution controls alone. We therefore propose a boundary-aware logic for interpreting ERW experiments: first identify what

compartment and accounting boundary an exchangeable Ca–Mg signal represents, then evaluate controllable levers within empirically supported domains and pair exchangeable-pool measurements with deeper soil, export or water-chemistry observations where CDR attribution requires open-system product transport.

2 Materials and Methods

2.1 The Ca-Mg proxy

Field closure of alkalinity or carbon mass balances is rarely feasible given sampling constraints and the cost of long-term monitoring, so ERW inference commonly relies on operational Ca^{2+} and Mg^{2+} signals measured in exchangeable pools, soil solution, or leachate (Amann & Hartmann, 2022). Because these Ca–Mg responses are among the most consistently reported treatment–control measurements, they provide a practical common currency for comparing relative ERW intensity across studies. Their interpretation, however, is conditional on the sampled compartment and integration window. In hydrologically connected soils, dissolution products can be diluted by background variability or exported beyond the sampled pool, weakening contrasts even when weathering proceeds (Cipolla et al., 2022). Detectability therefore constrains what field trials can conclude and how confidently cation signals can be translated into CDR (Hasemer et al., 2024). This helps explain why outcomes diverge across contexts and deployment choices, and why cross-study comparison improves when system boundaries and export pathways are made explicit (Holzer et al., 2023; Beerling et al., 2024; Reershemius et al., 2023).

Although Ca–Mg signals provide a practical common currency, cross-study inference is limited because deployment levers and environmental contexts are unevenly sampled across settings and rarely vary independently. Key design choices tend to co-occur in structured ways across the published record – a pattern partly imposed by the logistical and cost constraints of field experimentation (Swoboda et al., 2022): the energy and transport penalties of fine milling and heavy spreading constrain feasible PSD–dose combinations and monitoring durations, especially for field trials (Strefler et al., 2018). Lever effects can also be setting-dependent: grain-size influences are readily detected under controlled conditions, yet field signals can be reshaped by open-system transport and redistribution, complicating transfer from closed systems to real soils (Vanderkloot & Ryan, 2023). These considerations motivate a meta-regression framework that first identifies dominant controls within each setting and then tests

which effects persist once correlated covariates are accounted for. Comparability is further weakened by heterogeneous accounting scopes for translating ion signals into CDR (West et al., 2023).

To improve comparability of reported ERW CDR outcomes, Ca–Mg mobilisation is treated as a shared proxy for relative weathering intensity. The dataset comprises 81 peer-reviewed ERW studies published between 2018 and 2025 (205 treatment–control comparisons), with effect sizes quantified as log response ratios (lnRR) for exchangeable Ca, Mg and Ca+Mg. Evidence coverage is mapped across land use, feedstock group, PSD, application rate and study duration, and single- and multi-moderator random-effects meta-regression is used to identify controls that persist once correlated design choices are accounted for. Transferability is assessed by allowing hydroclimate proxies (rainfall and irrigation) to vary across experimental settings—from incubations and pots/mesocosms to field trials—testing whether sensitivities observed under controlled conditions persist in open agricultural systems. Eligible Δ(Ca+Mg) signals are also expressed in CDR units using a simple, consistent mass-balance conversion for cross-study comparison rather than site-level carbon auditing (Amann & Hartmann, 2022).

We note that exchangeable Ca and Mg are not diagnostic of silicate weathering alone: carbonate liming, fertiliser additions, and cation exchange can produce similar signals. Exclusion of carbonate-liming studies (criterion i) and the use of paired treatment–control designs reduce but do not eliminate this confounding; where co-inputs differ between treatment and control, residual bias in lnRR cannot be excluded and should be borne in mind when interpreting effect-size magnitudes.

2.2 Literature screening and data extraction

We conducted a systematic review to identify ERW studies reporting Ca and/or Mg dynamics following silicate rock amendments, to quantify weathering-driven cation responses and translate eligible signals into carbon dioxide removal (CDR). Searches (2018–2025) were performed in Web of Science, ScienceDirect, PubMed and Google Scholar using a harmonised Boolean string (Table S1). Searching and reporting followed PRISMA 2020 (Fig. S1) (Gusenbauer & Haddaway, 2020; Page et al., 2021). After de-duplication, two reviewers independently screened titles/abstracts and then full texts.

Studies were included if they (i) applied a silicate (or mixed silicate) feedstock to soil or sediment, (ii) included an untreated or conventionally managed control, (iii) reported extractable/exchangeable Ca and/or Mg in a measurable compartment enabling treatment–

control contrasts, and (iv) provided key context metadata where available (e.g., climate, initial pH, particle size, dose, duration, land use, feedstock, and setting). We excluded editorials, non-soil systems, modelling-only or paleoclimate studies, and carbonate liming without a silicate-weathering component. In total, 81 studies met these criteria (Table S2).

For each included study, we extracted treatment and control means, variance (SD/SE) and sample sizes for exchangeable/extractable Ca and Mg (and Ca+Mg where applicable). Figure-only values were digitised and cross-checked by two reviewers. All Ca and Mg data were harmonised to mmol kg^{-1} prior to effect-size calculation and EMB-based CDR conversion. We recorded site and design descriptors needed for moderator analyses (MAT, MAP, initial pH, feedstock/rock type, particle-size metric, application rate, duration, land use, and experimental setting). Land use was coded as upland cropland, lowland rice paddy, perennial grassland/forest, or bare-soil/abiotic reactors; setting as field, pot/mesocosm, or incubation/column. Where multiple depths or sampling dates were reported, we prioritised the surface layer (typically 0–20 cm) and the longest observation period. Where available, we also captured ΔpH, yield/biomass, inorganic carbon and author-reported CDR estimates for sensitivity checks.

2.3 Effect size calculation

To compare ERW-induced cation release across heterogeneous experimental designs, we used the natural log response ratio (lnRR) as the primary effect size (Lajeunesse, 2015). For each paired comparison between an ERW treatment and its corresponding control, lnRR was calculated as:

$$lnRR_X = \ln\left(\frac{\bar{X}_{treat}}{\bar{X}_{control}}\right)$$

where X denotes soil exchangeable Ca, Mg, or their sum (Ca + Mg), and mean treat and mean control are the reported means for the treatment and control, respectively. All Ca and Mg data were first converted to a common unit (mmol kg^{-1}), and only contrasts with strictly positive means in both groups were retained.

The sampling variance of each lnRR was derived from the associated standard deviations (SD) and sample sizes (n) following standard meta-analytic formulation:

$$v_{lnRR_X} = \frac{SD^2_{treat}}{(n_{treat} * \bar{X}^2_{treat})} + \frac{SD^2_{control}}{(n_{control} * \bar{X}^2_{control})}$$

When SE was reported, $SD = SE\sqrt{n}$. Effect sizes were inverse-variance weighted ($w_i = 1/v_i$) in all models. Contrasts were defined at the treatment level (unique feedstock/rock type, particle size, dose, land use and setting within each study). Where multiple depths or sampling dates were available, we prioritised the surface layer (typically 0–20 cm) and the longest observation period. Multiple contrasts per study were retained and within-study dependence was handled using multilevel models with study as a random effect.

2.4 Meta analysis

Overall lnRR and subgroup estimates were obtained using random-effects models, with residual heterogeneity quantified using Q and I^2. Analyses were implemented in R using metafor (Viechtbauer, 2010). Primary drivers were explored with single-moderator mixed-effects models. Continuous moderators were MAT, MAP, initial soil pH, particle size (log P80 or), application rate (log t ha^{-1}), and duration (log years). Categorical moderators were land use (upland cropland, lowland rice paddy, perennial grassland/forest, bare-soil/abiotic), feedstock/rock type (basalt, olivine, wollastonite, mixed silicates), experimental setting (field, pot/mesocosm, incubation/column), and soil texture (clayey, loamy, sandy). Covariate structure was summarised with Pearson correlations and PCA to diagnose collinearity and inform multivariate model specification (Supporting Information).

2.5 Meta-regression

To quantify joint controls on lnRR and to test whether climatic sensitivities differ across experimental settings, we fitted multivariate random-effects meta-regression models with a study-level random intercept(Assink & Wibbelink, 2016). In notation, $lnRR_i$ was expressed as:

$$lnRR_i = \beta_0 + \Sigma_k \beta_k X_{k,i} + u_j[_i] + \varepsilon_i,$$

where $X_{k,i}$ are moderator values for treatment i, $u_j[_i]$ is a random intercept for study j, and ε_i is the sampling error with variance v_lnRR derived. Four concept-driven “forcing bundles” were considered: (1) chemical forcing, combining application rate (hereafter Dose) with initial soil pH and reported ΔpH; (2) physical forcing, combining Dose, particle size and soil texture; (3) application background, combining rock type with pH and texture; and (4) climate superposition, combining water supply (MAP or experimental water input), MAT and experiment type/setting. Results are reported in Section 3 using these same bundle labels, with Fig. 4 summarising explained-heterogeneity partitioning and setting-stratified coefficients (full model specifications and alternative bundle tests are provided in the Supporting Information).

Within each bundle we fitted main effects and, where ecologically interpretable, two-way interaction terms to allow sensitivities to vary across experimental openness.

Within each forcing bundle, prespecified nested extensions (main effects, then interpretable interactions) were evaluated using likelihood-ratio tests, with AICc used to compare alternative specifications. Model performance was summarised by the reduction in residual between-study heterogeneity (tau-squared, τ^2) relative to the intercept-only model and expressed as pseudo-$R^2 = 1 - (\tau^2\_model / \tau^2\_0)$. To assess independent explanatory power under correlated covariates, we computed conditional contributions using a drop-one approach (Δ pseudo-R^2_j = pseudo-R^2_full − pseudo-R^2_without j). This was applied to a 10-factor framework spanning process variables (Dose, particle-size proxy, ΔpH, temperature, water input, duration) and design/environment descriptors (rock type, soil type, experiment type, plant presence). Multivariate models were fitted to the subset of effect sizes with complete covariate information; model-specific sample sizes are reported alongside corresponding figures and tables.

2.6 Conversion from Δ(Ca+Mg) to apparent retained CO_2-equivalent signal

For studies reporting treatment–control differences in exchangeable Ca and Mg, we applied an elementary mass-balance (EMB) scaling to express retained exchangeable signals as CO_2-equivalent weathering-product pools. With Δ(Ca+Mg) in mmol kg^{-1} and assuming 0–20 cm sampling depth and bulk density of 1.3 g cm^{-3} (2.6×10^6 kg soil ha^{-1}), the retained exchangeable Ca+Mg pool was converted using divalent-cation silicate-weathering stoichiometry. Under this stoichiometric approximation, 1 mol of exchangeable Ca^{2+} or Mg^{2+} is treated as equivalent to 1 mol of CO_2 consumption. The apparent retained CO_2-equivalent pool was therefore calculated as:

$$CDReq\_exch,0–20\ cm\ (t\ CO_2\ ha^{-1}) = 0.1144 \times \Delta(Ca+Mg),$$

where Δ(Ca+Mg) is the treatment–control difference in exchangeable Ca+Mg in mmol kg^{-1}. The apparent annualised retained signal was calculated as:

$$CDReq\_exch,yr = (365 / T) \times CDReq\_exch,0–20\ cm\ ,$$

where T is duration (days). This EMB conversion is used as a harmonised scaling of the retained 0–20 cm exchangeable Ca+Mg signal, not as a full net-CDR audit or a measure of whole-system carbon removal. Because it is anchored to the sampled near-field exchangeable pool, it does not capture weathering products redistributed below 20 cm, exported in drainage

or surface water, incorporated into biomass or secondary phases, or otherwise transformed outside the measured compartment.

2.7 Evidence-supported operating envelopes (ESO)

To avoid over-interpreting model optima in poorly sampled covariate space, we mapped evidence-supported operating envelopes (ESOs) for key controllable levers (e.g., dose × particle size; baseline pH × particle size). For each response and setting, we fit the multivariable meta-regression and predicted the response over a regular grid spanning the observed covariate ranges. We then quantified empirical support as the local data density in this covariate plane (Gaussian kernel density estimate, KDE) and quantified predictive reliability as the precision of the predicted mean (standard error from the fitted model). Grid cells were retained as the ESO only where both conditions were met: KDE exceeded a low-density threshold and prediction uncertainty was below a high-uncertainty threshold (both defined by within-plane quantiles). All reported "high-response" regions were therefore interpreted only within the ESO, and predictions outside the ESO were treated as extrapolations.

3 Results

3.1 Exchangeable Ca–Mg signals weaken with experimental openness

Across the outlier-screened dataset, ERW amendments produced a clear treatment–control signal of divalent base-cation mobilisation in the exchangeable pool. Pooled effects were positive for both ions but asymmetric: exchangeable Ca increased modestly (lnRR = 0.18; ~+20%), whereas exchangeable Mg increased more strongly (lnRR = 0.43; ~+54%). Paired Ca–Mg contrasts further show that Mg responses exceed Ca in most comparisons (Fig. 1). Importantly, this Mg–Ca separation becomes most evident as systems become more open: the Ca signal attenuates and appears less consistently retained/detectable under open (field) conditions, whereas Mg remains more robust. For downstream synthesis we therefore use the charge-equivalent composite Ca+Mg (pooled lnRR ≈ 0.29; ~+33%) as a harmonised proxy for relative weathering intensity that preserves the direction of both single-ion responses while reducing sensitivity to ion-specific instability.

Setting stratification supports an openness-dependent retention/detectability control. For Ca, pooled effects were smallest in field trials (lnRR = 0.12; ~+13%), intermediate in pot/mesocosm studies (lnRR = 0.42; ~+52%), and largest in incubations/soil reactors (lnRR =

0.67; ~+95%). Mg showed the same ordering but a notably weaker attenuation with openness (field: lnRR = 0.40; ~+49%; pot/mesocosm: lnRR = 0.55; ~+73%; incubations/soil reactors: lnRR ≈ 0.63; ~+88%). Incubation estimates were more sensitive to a small number of high-influence contrasts, consistent with clustered design space and smaller effective sample size; under conservative handling of extremes they converged to lnRR ≈ 0.63 (~+88%). Because evidence is geographically/climatically clustered and deployment choices occupy a constrained region of covariate space (Fig. S3), setting comparisons are most defensible where empirical coverage is densest.

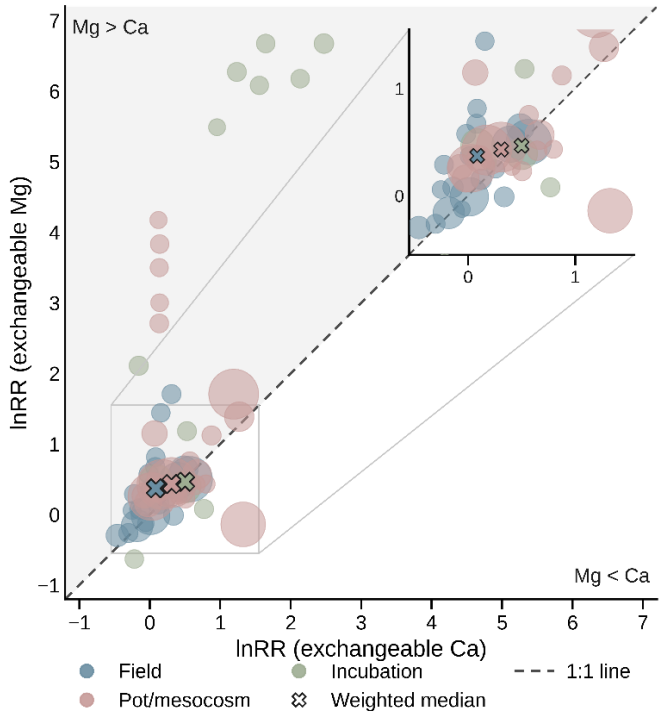

Fig. 1. Exchangeable Mg versus Ca response signals across ERW studies. Points show treatment–control contrasts plotted as lnRR(exchangeable Mg) versus lnRR(exchangeable Ca), with symbol area scaled by study weight and colours denoting setting (field, pot/mesocosm, incubation). The dashed 1:1 line indicates equal responses (Mg = Ca); values above the line indicate stronger Mg mobilisation. Crosses mark weighted medians for each setting and ellipses show 95% data ellipses. Insets magnify the dense central cluster. lnRR = ln(treatment/control).

Using Ca+Mg as a unified metric, treatment-driven Δ(Ca+Mg) from the 0–20 cm exchangeable pool exhibited a small and strongly right-skewed distribution (Fig. S3): most comparisons were near zero and <0.1 t CO_2 ha^{-1} yr^{-1}, with a limited upper tail extending to ~0.6. Setting-specific means were ~0.034 (field) and ~0.062 t CO_2 ha^{-1} yr^{-1} (pot/mesocosm) within the exchangeable topsoil pool measured in most field trials. Benchmarks reported under broader accounting boundaries are not directly comparable, but illustrate the magnitude gap that scope differences can create (Baek et al., 2023; Beerling et al., 2024; Table S2). The exchangeable-pool

conversion therefore captures an apparent retained topsoil signal. It should not be interpreted as whole-system CDR because it does not include products redistributed below the sampled layer, exported hydrologically, incorporated into biomass or secondary phases, or otherwise transformed outside the measured compartment.

Consistent with alkalinity generation, soil pH increased following ERW (mean ΔpH ≈ +0.66; median ≈ +0.41), with larger ΔpH more frequently reported in incubations than in pots or field trials. Across settings, larger ΔpH generally coincided with larger increases in exchangeable Ca+Mg (Fig. 1), supporting internal consistency between alkalinity shifts and the ion-release proxy. Uncertainty expands at high ΔpH where observations are sparse and fitted relationships become increasingly influenced by a small number of comparisons (Fig. S4).

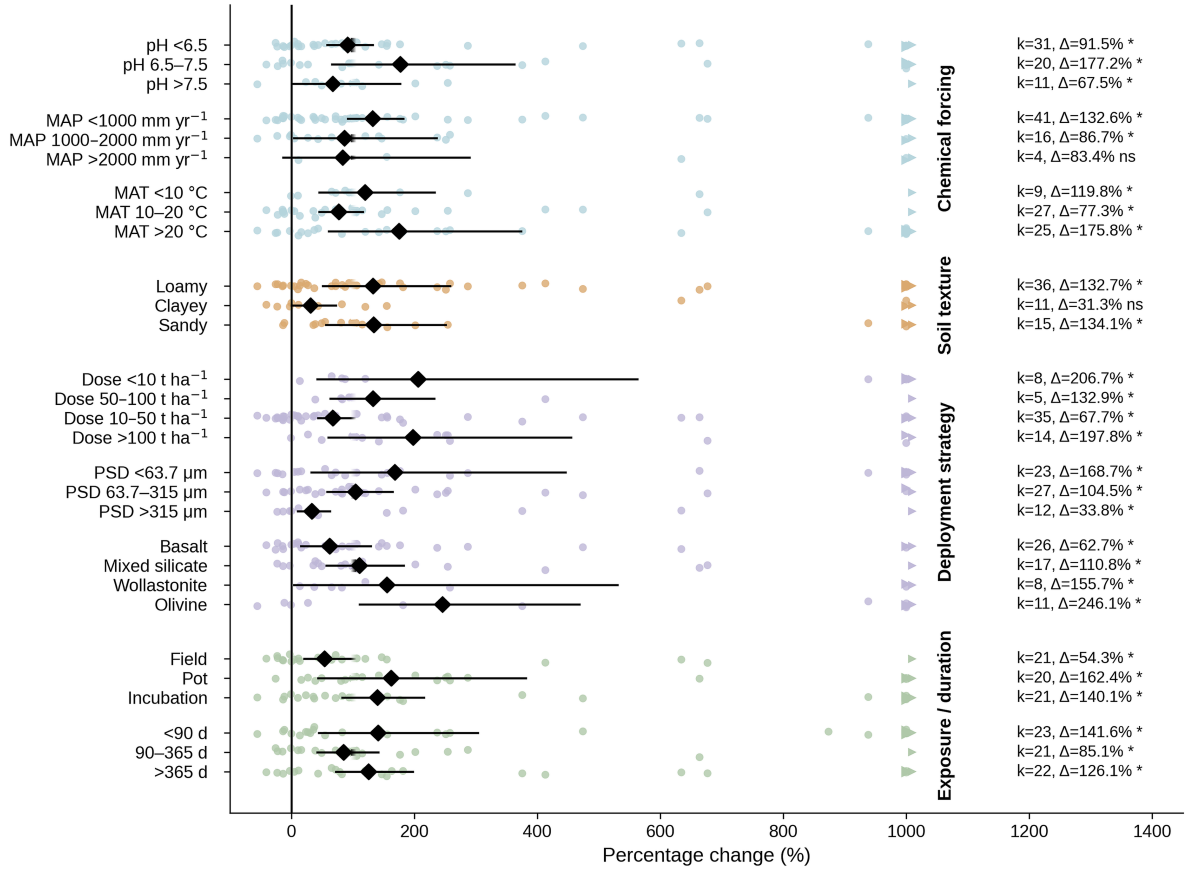

Fig. 2. Categorical moderators of ERW effects on retained exchangeable Ca+Mg responses. Subgroup meta-analyses are shown for baseline pH, mean annual precipitation (MAP), mean annual temperature (MAT), soil texture, application rate, particle size distribution (PSD), rock type, experimental setting, and exposure duration. Coloured points represent individual treatment–control contrasts, expressed as percentage change (exp (lnRR) − 1) × 100. Black diamonds indicate pooled subgroup effects and horizontal bars denote 95% confidence intervals. The vertical reference line at 0% indicates no change relative to the control. For each subgroup, *k* is the number of contrasts and Δ is the pooled percentage change; * denotes $P < 0.05$ and ns indicates non-significance. Right-pointing triangles at the plotting limit indicate observations exceeding the displayed x-axis range.

3.2 Broad patterns and structured heterogeneity across the evidence base

Single-moderator models indicate structured heterogeneity in lnRR(Ca+Mg) across experimental setting, exposure time, chemical context and deployment choices (Fig. 2). Across binned summaries, responses were positive in most strata but were smallest in field trials (Δ = 54.3%; k = 21) and larger in pots (Δ = 162.4%; k = 20) and incubations (Δ = 140.1%; k = 21) (Fig. 2). Exposure duration also showed structured variation, but not a monotonic increase with time: responses were positive across all duration bins and were lowest at 90–365 d (Δ = 85.1%; k = 21), while estimates were higher at <90 d (Δ = 141.6%; k = 23) and >365 d (Δ = 126.1%; k = 22) (Fig. 2).

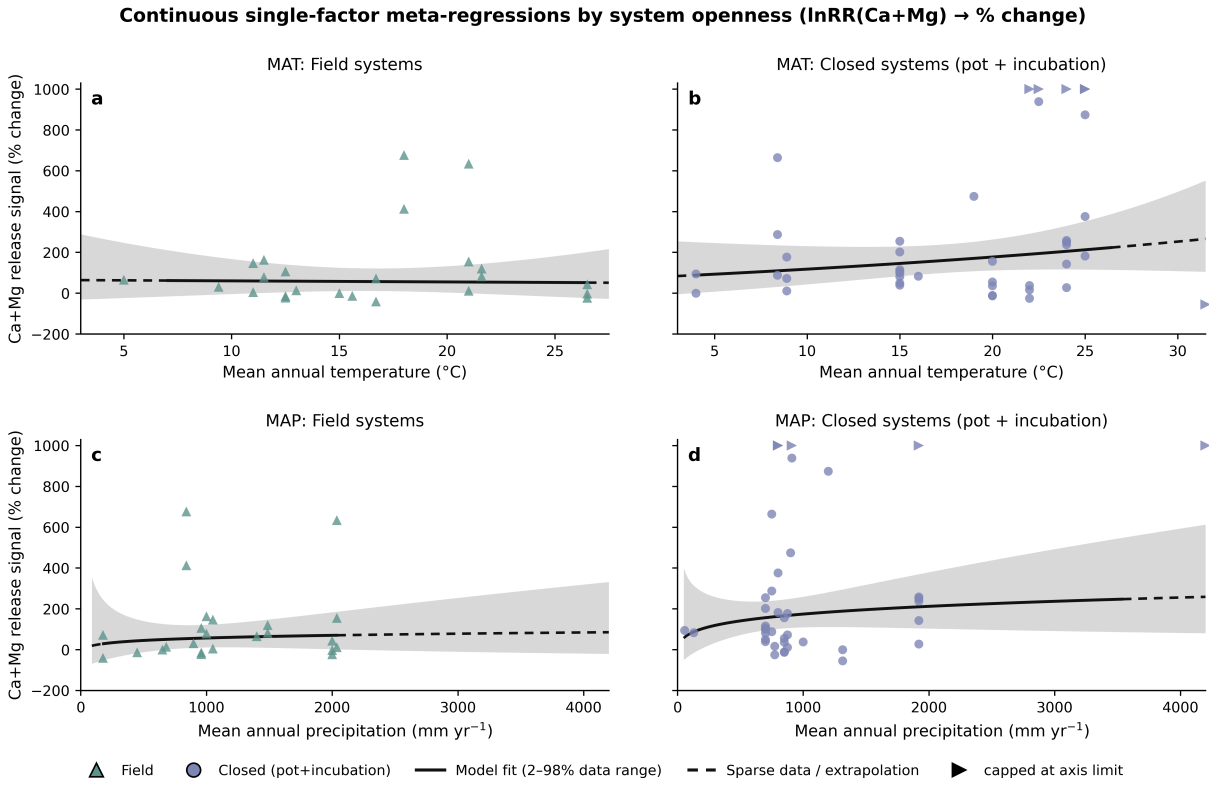

Fig. 3. Climatic covariates associated with exchangeable Ca+Mg responses in field and systems.

Relationships between Ca+Mg release signal, expressed as percentage change converted from lnRR(Ca+Mg), and mean annual temperature (MAT; a,b) or mean annual precipitation (MAP; c,d), shown separately for field systems and closed systems (pot + incubation). Points represent individual observations. Black lines show fitted single-factor meta-regressions, with solid segments indicating the 2–98% data range and dashed segments indicating sparse or extrapolated regions. Grey shading represents 95% confidence intervals. Triangles on the plotting boundaries indicate observations exceeding the displayed x- or y-axis limits. Panels c and d are shown on a common linear MAP axis to improve interpretability and comparability between field and closed systems; the broader high-water-input range in closed systems reflects a small number of experimental high-precipitation treatments. The fitted MAP meta-regressions remain based on log10-transformed MAP.

Chemical context emerged as a recurrent axis of variation. Across baseline pH bins, lnRR(Ca+Mg) remained positive and peaked at intermediate pH (pH <6.5: Δ = 91.5%, k = 31; pH 6.5–7.5: Δ = 177.2%, k = 20; Fig. 2), with smaller and less certain effects at higher pH

where empirical support is sparse (pH ≥7.5: Δ = 67.5%, k = 11). Consistent with this pattern, lnRR(Ca+Mg) increased with realised ERW-induced ΔpH (post–pre) across settings (Fig. S4), although uncertainty widens at high ΔpH where observations are limited.

Climate covariates also co-varied with lnRR(Ca+Mg), but apparent sensitivities depended on experimental setting (Fig. 3). Across precipitation bins, effects were positive in dry–intermediate classes, while the wettest class remained positive but uncertain (MAP >2000 mm yr^{-1}: Δ = 83.4%, k = 4; Fig. 2). Temperature bins suggested larger responses in warmer climates (MAT >20 °C: Δ = 175.8%, k = 25; Fig. 2). When stratified by setting, climate–response slopes were weak in field datasets but strengthened in more controlled settings (pots + incubations), indicating limited transferability of hydroclimate sensitivities inferred from semi-controlled studies to open field conditions (Fig. 3).

Deployment levers produced sizeable contrasts while also revealing non-orthogonal designs in the literature. Olivine showed the largest mean increase (Δ = 246.1%, k = 11), whereas basalt was smaller (Δ = 62.7%, k = 26; Fig. 2). Dose bins were uniformly positive yet not monotonic (<10 t ha^{-1}: Δ = 206.7%, k = 8; >100 t ha^{-1}: Δ = 197.8%, k = 14), consistent with sparse coverage and co-variation with other design choices. PSD classes showed a clearer gradient (coarse >315 μm: Δ = 33.8%, k = 12; fine <63.7 μm: Δ = 168.7%, k = 23), consistent with continuous single-moderator fits (Fig. 2). Soil texture further modulated outcomes, with smaller and uncertain means in clayey soils (Δ = 31.3%; k = 11) relative to loamy and sandy classes (Fig. 2). Notably, climate, baseline context and deployment variables (dose, PSD and setting) co-vary across studies (Fig. S7), so these single-moderator contrasts are first-order patterns rather than independent effects (Fig. S5). Multivariate models therefore act as a robustness check, testing which effects persist under correlated covariates and across settings.

3.3 Robust controls under joint adjustment differ between settings

Setting-stratified multivariable REML meta-regressions show that the conditional control structure of exchangeable base-cation signals shifts systematically along an openness gradient (field → pot/mesocosm → incubation; Fig. 4). Models are fit separately by setting and ion pool (Ca, Mg, Ca+Mg), with standardised coefficients (β) reported alongside 95% confidence intervals, conditional contributions (ΔR^2), and setting-specific explanatory power. For interpretation, predictors are grouped into four concept-aligned families that map onto Fig. 4: chemical context (baseline pH), lever tuning (dose, particle size), hydroclimate superposition (water input, temperature) and integration time (duration). Across the gradient, the conditional

structure contracts from multi-driver signatures in closed systems to a sparse, lever-resolved signature in the field evidence base, consistent with increasing decoupling of exchangeable pools from system-scale fluxes under open boundaries.

For the harmonised Ca+Mg proxy, the field subset resolves a predominantly lever-driven structure ($R^2 = 0.41$; $n = 24$), with dose the dominant retained predictor ($\beta = 0.68$, $P = 2.7\times10^{-4}$; $\Delta R^2 \approx 0.52$) and other terms contributing comparatively little incremental information (Fig. 4i). In pots/mesocosms ($R^2 = 0.43$; $n = 24$), conditional controls broaden and become boundary-sensitive: water input is retained as a strong positive predictor ($\beta = 1.46$, $P = 0.005$) while temperature is negative ($\beta = -0.89$, $P = 6.5\times10^{-4}$), with additional retained contributions from duration ($\beta = -3.28$, $P = 0.015$) and particle size ($\beta = 2.29$, $P = 0.023$) (Fig. 4h). In incubations ($R^2 = 0.93$; $n = 27$), conditional structure is strongest and aligns with chemistry and integration: baseline pH is strongly negative ($\beta = -3.25$, $P < 10^{-12}$) and duration strongly positive ($\beta = 2.17$, $P = 2.3\times10^{-9}$), with dose and temperature also retained (Fig. 4g).

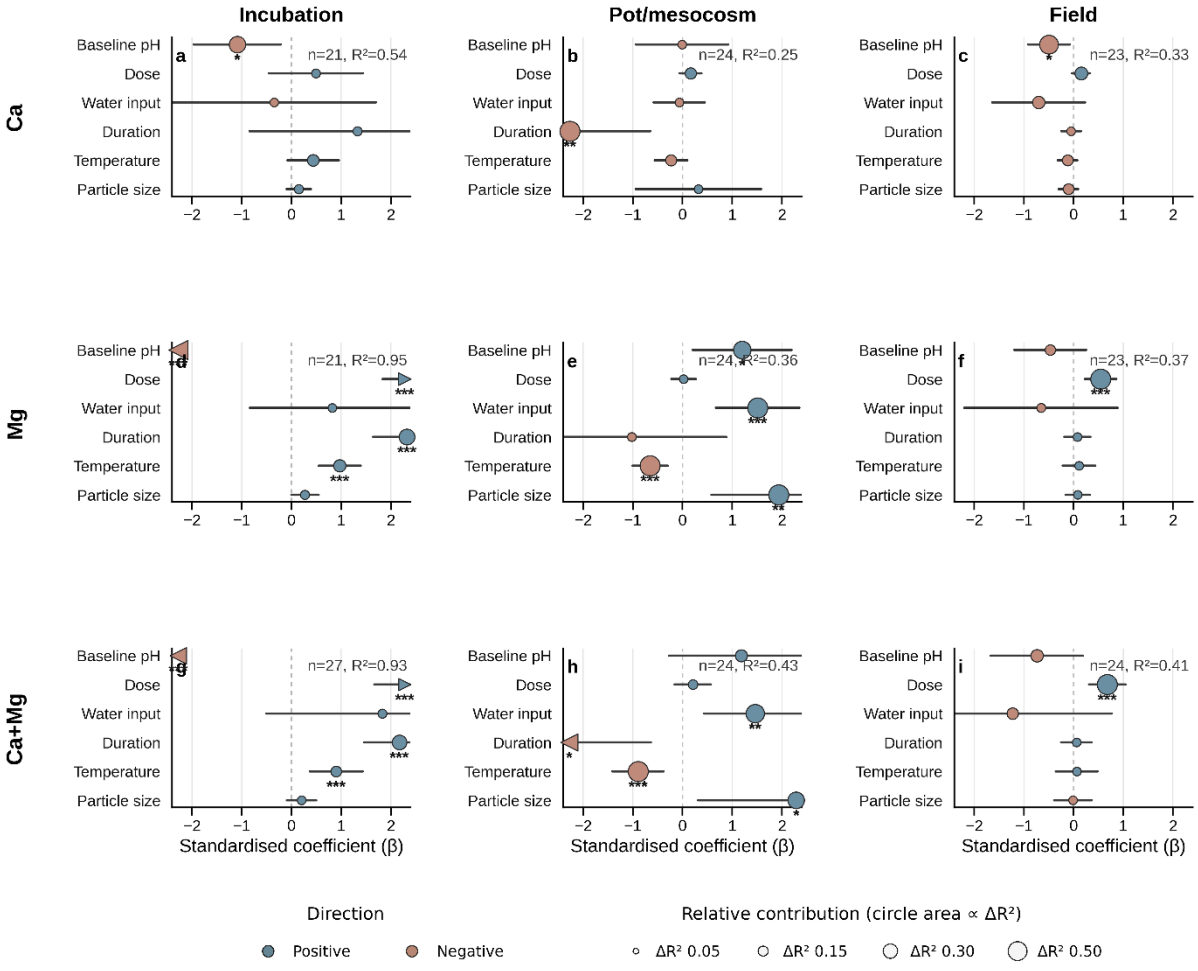

Fig. 4. Multivariable controls on exchangeable base-cation signals across settings. Standardised coefficients (β) from multivariable models are shown for exchangeable Ca, Mg and Ca+Mg responses (rows) across

incubations, pot/mesocosm studies and field trials (columns). Points show β estimates and bars show 95% confidence intervals (dashed line, β = 0). Colour indicates effect direction, and circle area is proportional to each predictor's relative contribution to model fit (ΔR^2), using a common size scale across all panels. Triangles at the plotting limits indicate estimates that extend beyond the displayed x-axis range. Asterisks denote significance (*P < 0.05, **P < 0.01, ***P < 0.001); panel annotations report n and model R^2.

Ion-specific fits sharpen the "currency" contrast. Mg exhibits the most openness-consistent conditional structure: field Mg is again dose-dominated (β = 0.55, P = 7.4×10^{-4}; R^2 = 0.37; n = 23; Fig. 4f), pots retain strong hydroclimate sensitivity (water input β = 1.51, P = 4.3×10^{-4}; temperature β = −0.65, P = 3.1×10^{-4}; Fig. 4e), and incubations mirror Ca+Mg with strongly negative pH and strongly positive duration (Fig. 4d). By contrast, Ca is less lever-resolved and more setting-specific (R^2 = 0.25–0.54): field Ca is primarily pH-structured (consistent with Ca mobility in field soils being governed more strongly by cation exchange dynamics than by dissolution flux; β = −0.49, P = 0.021; Fig. 4c), pot Ca is dominated by a duration term (β = −2.27, P = 0.006; Fig. 4b), and incubation Ca retains only a modest negative pH association (β = −1.09, P = 0.015; Fig. 4a).

Across settings, ΔR^2 patterns reinforce that openness governs detectability: closed systems preserve multi-driver signatures (chemistry × integration time × hydroclimate), whereas open field systems preferentially retain a lever-indexed signal, most clearly expressed for Mg and Ca+Mg. Because predictors co-vary across the literature and the field evidence base is comparatively thin, coefficients and ΔR^2 values are interpreted as conditional associations rather than independent causal effects, motivating the evidence-bounded operating-envelope analyses that follow.

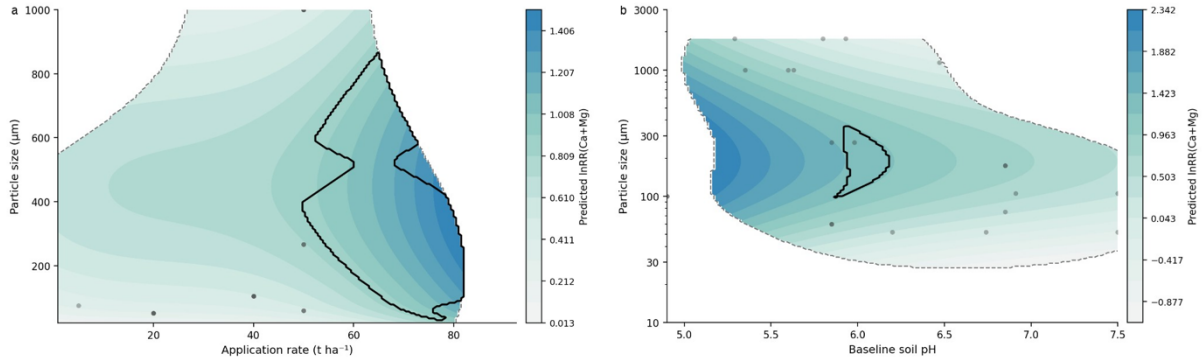

Fig. 5. Evidence-bounded operating envelopes for field exchangeable Ca+Mg signals. Predicted lnRR(Ca+Mg) from the field-only multivariable REML meta-regression is mapped across (a) application rate (t ha^{-1}) × particle size (µm) and (b) baseline soil pH × particle size (µm). Shading shows modelled responses, and points indicate observed study covariate combinations. Dashed outlines delimit the evidence-supported covariate

space, and the thick black contour marks the evidence-bounded high-response region used to define defensible optimisation targets.

3.4 Evidence-supported operating envelopes constrain optimisation and deployment inference

Fig. 5 places the field lever patterns within an evidence-bounded design space—application rate (dose) and reported particle size—and shows how their incremental explanatory power depends on experimental setting and signal currency. Here, "detectability" means that a lever remains identifiable under joint adjustment, through non-trivial conditional contribution (ΔR^2) and/or a retained, significant coefficient in setting-stratified multivariable models (Fig. 4). In the field evidence base, lever information concentrates in dose for exchangeable Mg and the Ca+Mg composite (Mg: $\Delta R^2 \approx 0.47$, $P < 0.001$; Ca+Mg: $\Delta R^2 \approx 0.50$, $P < 0.001$), whereas particle size contributes little incremental information (Fig. S6). For exchangeable Ca, neither dose nor particle size is consistently supported across settings (ΔR^2 generally $\lesssim 0.15$; Fig. 4). These results indicate that, within the current field evidence base, application rate is the dominant and best-resolved controllable design variable for retained exchangeable Mg and Ca+Mg responses, while Ca remains weakly lever-resolved.

Lever signatures shift in semi-controlled settings. In pot/mesocosm datasets, particle size is retained for Mg and Ca+Mg under joint adjustment (Mg: $\Delta R^2 \approx 0.32$, $P < 0.01$; Ca+Mg: $\Delta R^2 \approx 0.19$, $P < 0.05$), while dose is not retained (Fig. 4). In incubations, dose is again retained for Mg and Ca+Mg ($\Delta R^2 \approx 0.08$, $P < 0.001$), whereas particle-size effects remain weak (Fig. 4). This yields a setting-dependent lever hierarchy: dose structures detectable field Mg and Ca+Mg signals; particle-size effects are most apparent in pots/mesocosms; and neither lever is robustly resolved for Ca across settings.

Fig. 5 then places these lever patterns within an evidence-bounded field design space for Ca+Mg. Predicted lnRR(Ca+Mg) varies across the dose–particle size plane (Fig. 5a) and the baseline pH–particle size plane (Fig. 5b), but empirical support is uneven. The dashed outline marks the data-supported domain, while the ESO (solid outline) retains only grid cells with sufficient local data density (Gaussian KDE) and bounded prediction uncertainty (standard error of the predicted mean; thresholds defined by within-plane quantiles). High predicted responses often extend into low-support or high-uncertainty regions, so defensible optimisation claims are restricted to the ESO. Within this supported domain, variation aligns mainly with dose, consistent with its dominance in the field models (Fig. 4).

4 Discussion

4.1 Experimental openness as a key constraint on field signal interpretability

Across the compiled evidence base, retained exchangeable Ca–Mg responses are generally positive but strongly heterogeneous, and this heterogeneity is not captured by a single "warmer–wetter–finer–higher dose" heuristic. Instead, our meta-analysis shows that exchangeable signal detectability in the sampled compartment is a primary limitation on what can be concluded from field trials. Specifically, pooled treatment–control contrasts systematically weaken along an openness gradient (incubation → pot/mesocosm → field; Section 3.1), and Mg and Ca+Mg provide more consistently detectable exchangeable signals than Ca across settings (Section 3.1; Fig. 2). This pattern implies that cross-study comparability is limited not only by dissolution potential, but also by whether weathering products remain detectable within the measured pool during the integration window, rather than being redistributed below the sampling depth or exported before they are captured as an exchangeable signal**.**

Joint models further show that the apparent "principal controls" shift once correlated design and context are accounted for. Single-moderator trends are broadly positive across many strata (Section 3.2), but multivariable attribution concentrates explanatory power in a smaller set of predictors and reveals strong setting dependence (Section 3.3). In particular, within the current field evidence base, dose is the dominant and best-resolved controllable design variable for retained exchangeable Mg and Ca+Mg, whereas PSD lever effects are primarily supported in pot/mesocosm studies and are not independently robust in field subsets once covariate structure is controlled (Fig. 4). These results motivate a distinction between *controllable levers* and *context filters* in interpreting exchangeable-pool outcomes.

A related constraint is that model-predicted response maxima are often not the same as evidence-supported operating space. ESO diagnostics make this explicit: fitted response surfaces extend into sparsely supported covariate regions, and restricting inference to domains with empirical coverage and bounded predictive uncertainty substantially contracts the space in which optimisation claims are defensible (Fig. 5a,b). The following sections therefore interpret the evidence through an evidence-weighted lens that prioritises portability across settings, separates lever effects from context dependence, and treats empirical support as a prerequisite for boundary-aware field interpretation.

4.2 Lever hierarchy under field conditions: dose leads, with pH and time as context filters

Across settings, multivariable attribution identifies a compact set of chemical and time-integration terms that most consistently structure exchangeable Ca–Mg responses. In the field evidence base, dose emerges as the leading controllable lever for exchangeable Mg and Ca+Mg, whereas other candidate levers are weaker or setting-contingent once covariate structure is accounted for (Sections 3.3–3.4; Fig. 4). This result aligns with the practical constraint that application intensity sets the magnitude of the measurable treatment–control contrast under typical field sampling scopes, even when absolute reaction progress cannot be closed with full alkalinity or carbon mass balances (Hartmann et al., 2013; Beerling et al., 2020).

A second recurrent constraint is chemical headroom, captured by baseline pH and buffering context. Across the compiled dataset, baseline pH is associated with systematic shifts in exchangeable Ca–Mg contrasts, but its influence is most clearly resolved where controlled designs reduce background variability and confounding (Sections 3.2–3.3). Consistent with this, exchangeable Ca shows stronger pH-structured behaviour than Mg in several setting-stratified fits, while Ca+Mg integrates both ions and yields a more stable comparison currency across studies. Because covariates co-vary non-randomly in the published record, baseline pH patterns are interpreted here as conditional constraints on signal expression rather than standalone, universally transferable controls (Fig. S2). Realised ΔpH provides a complementary, high-information indicator of signal maturity. Across studies, larger ERW-induced ΔpH tends to co-occur with larger lnRR(Ca+Mg), indicating that where acid–base state shifts measurably within the observation window, exchangeable Ca–Mg contrasts are more likely to emerge above background variability. ΔpH is therefore most useful as a progress proxy for comparing the maturity and interpretability of trial outcomes across heterogeneous contexts, rather than as a deployable lever.

Finally, duration sets the integration window required for exchangeable accumulation to separate from background variability. In the single-moderator summaries, duration bins were positive but non-monotonic, with the lowest binned estimate occurring at 90–365 d rather than <90 d. Together, dose (supply), baseline pH (headroom), ΔpH (progress) and duration (integration) define an evidence-weighted quartet that predicts when exchangeable Ca–Mg signals—especially the Ca+Mg composite—are most likely to be detectable and comparable, and provides the basis for separating lever tuning from context screening in boundary-aware field interpretation.

4.3 Sensitivities do not transfer cleanly from controlled studies to fields

Setting-stratified models show that sensitivities inferred from controlled studies do not transfer uniformly to field conditions, and this non-transferability is amplified by the way the evidence base is sampled. The design-space PCA (Fig. S7) makes this explicit: key context variables (MAT/MAP, baseline pH) and deployment choices (dose, PSD, duration) occupy a structured, correlated space rather than an orthogonal design. As a result, single-factor patterns can conflate leverage with context and setting, motivating interpretation that is conditional on both openness class and empirical coverage.

Under joint adjustment, hydroclimate terms are weakly resolved in the field subset for Mg and Ca+Mg relative to controlled and semi-controlled datasets, indicating that climate–response relationships observed in incubations or pots do not translate as a stable field signal within the exchangeable pool. A similar setting filter applies to particle size. While PSD emerges as an identifiable modifier in pot/mesocosm models for Mg and Ca+Mg, it is not retained as an independently robust field lever once covariate structure is accounted for (Sections 3.3–3.4; Fig. S6). In contrast, field models concentrate lever structure in application rate for Mg and Ca+Mg, consistent with the field evidence base supporting application rate as the most reproducible controllable lever for retained exchangeable signals under current monitoring scopes.

4.4 Limitations of the current evidence base

This synthesis is constrained by the way ERW trials are currently reported and by the limited size and uneven coverage of field datasets relative to controlled studies. Field meta-regressions therefore capture conditional associations within a narrow, correlated design space (dose, particle size, duration and context rarely vary independently) and should not be interpreted as identifying universal optima. In addition, our harmonised Δ(Ca+Mg)-based EMB scaling represents an apparent retained CO_2-equivalent signal anchored to the 0–20 cm exchangeable pool and is not a whole-system CDR audit; export, redistribution and secondary mineral formation can shift products outside the sampled compartment and decouple retained exchangeable signals from whole-system weathering-product fate. These limitations reinforce the need for boundary-aligned trial designs and paired soil–water measurements when the aim is boundary-aligned CDR attribution**.**

4.5 CDR-oriented screening and boundary-aware signal interpretation

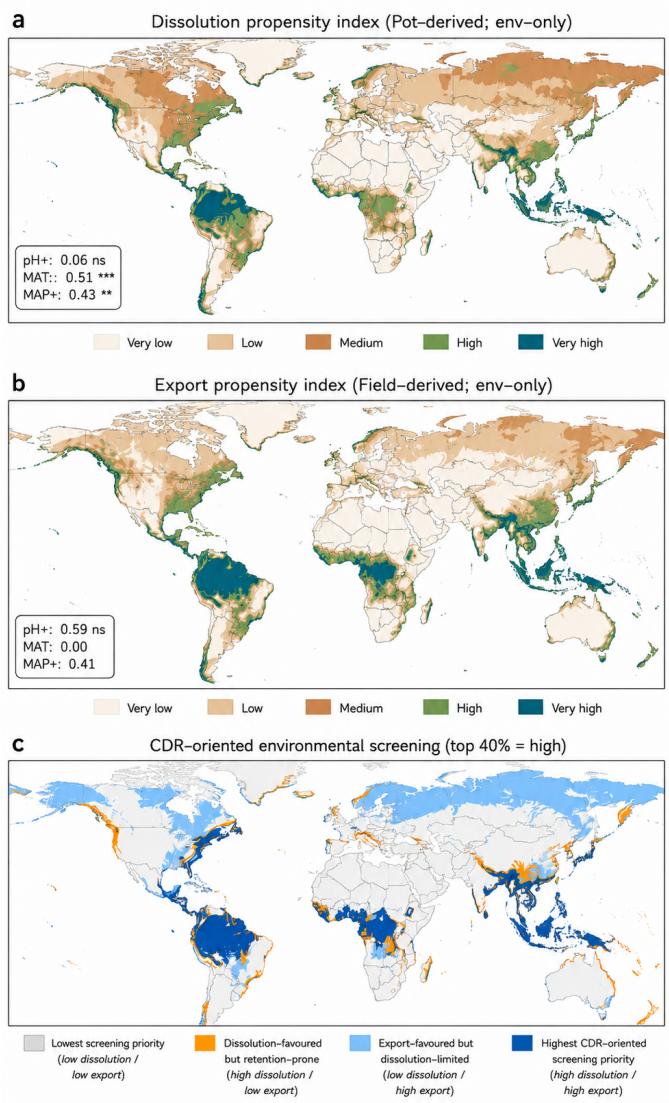

Figure 6. Global environmental screening of dissolution and export propensity for enhanced rock weathering (ERW). a. Pot-derived, environment-only dissolution propensity index projected from meta-regression moderators, including baseline soil pH, mean annual temperature (MAT) and mean annual precipitation (MAP). Higher values indicate conditions associated with stronger dissolution-related Ca–Mg responses. **b.** Field-derived, environment-only export propensity index. Because most field studies report only upper 0–20 cm exchangeable Ca and Mg, predicted near-field retention was inverted so that higher values indicate lower shallow retention and greater potential for redistribution or hydrological export. **c.** CDR-oriented environmental screening based on the overlap between high dissolution and high export propensity, with high values defined as the top 40% of each index. These maps are intended as evidence-weighted environmental screening layers rather than estimates of realised CDR or prescriptions for deployment.

The results of this synthesis show that experimental openness is not merely a design descriptor, but a control on which part of the weathering-product fate is observed. As systems become more hydrologically connected, a weak or absent 0–20 cm exchangeable Ca–Mg signal may reflect redistribution below the sampled layer or hydrological export, rather than limited silicate dissolution. Conversely, a strong near-field exchangeable signal indicates retention of weathering products within the sampled compartment, but does not by itself quantify exported

alkalinity or durable CDR. The same underlying weathering process can therefore lead to different interpretations depending on whether the measurement boundary captures retention, redistribution or export.

Fig. 6 translates this boundary-aware interpretation into an environmental screening framework. The pot-derived dissolution propensity index identifies environments where stronger dissolution-related Ca–Mg responses are more likely under controlled or semi-controlled boundaries. The field-derived export propensity index is interpreted differently: because most field studies report only shallow exchangeable-pool data, lower retained 0–20 cm Ca+Mg signals are used as a proxy consistent with greater redistribution or export propensity, rather than as direct evidence of weaker weathering. Combining these indices highlights environments where high dissolution propensity coincides with high export propensity, which we interpret as priority areas for follow-up boundary-aligned CDR assessment, not as quantified CDR estimates. Conversely, high dissolution combined with low export propensity is interpreted as dissolution-favoured but retention-prone. These maps should therefore be read as evidence-weighted environmental screening layers, not as realised CDR estimates or deployment prescriptions.

Fig. 7 then converts this interpretation into a practical decision rule for reading exchangeable cation signals. Rather than treating exchangeable Ca–Mg accumulation as a universal indicator of ERW performance, the figure first asks what boundary the signal represents, then links that boundary to the appropriate design levers and measurement package. This workflow separates near-field retention, product partitioning and open-field CDR attribution, and therefore avoids equating either high retained exchangeable Ca–Mg or low topsoil detection with whole-system CDR.

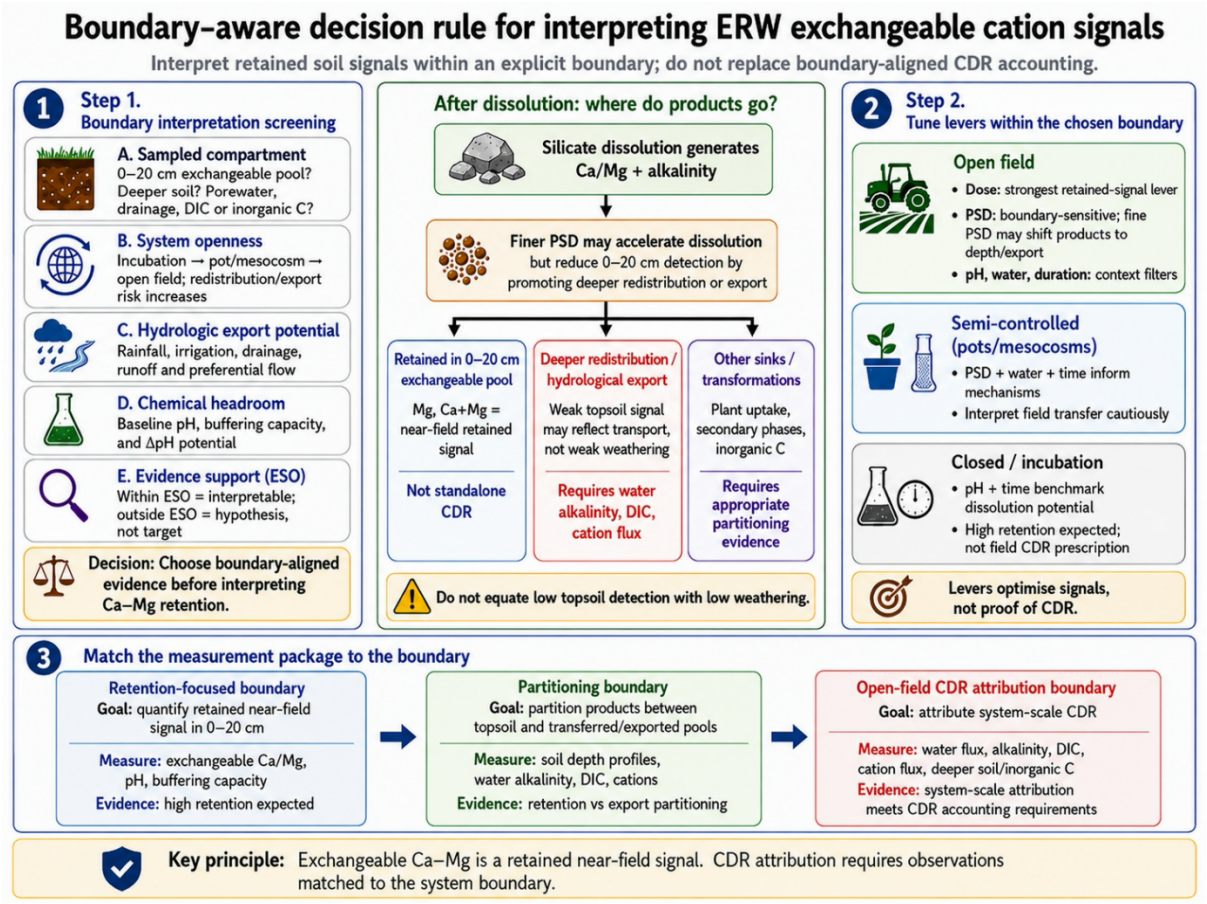

Figure 7. Boundary-aware decision rule for interpreting ERW exchangeable cation signals. Step 1 identifies the measurement boundary within which a treatment–control exchangeable Ca–Mg response should be interpreted, considering the sampled compartment, integration window, baseline chemical headroom, hydrologic connectivity and empirical support. Step 2 evaluates controllable design variables within that boundary, emphasising application rate in field settings and treating PSD and hydroclimate sensitivities as boundary-dependent. Step 3 matches the measurement package to the accounting objective, distinguishing retention-focused measurements, product-partitioning measurements and open-field CDR attribution. Low near-surface exchangeable detection, including under finer-PSD treatments, should therefore be interpreted cautiously in the absence of depth-profile or water-chemistry constraints.

The PSD result illustrates why this decision rule is needed. In controlled or semi-controlled settings, finer PSD is associated with stronger retained exchangeable Ca, Mg and Ca+Mg responses, consistent with a more direct expression of surface-area-driven dissolution where hydrological export is constrained. In field settings, however, this positive PSD signal is not expressed in the same way in the 0–20 cm exchangeable pool; for retained Ca+Mg, the field association is weak and, in some models, negative under joint adjustment. This contrast should not be read as evidence that finer material is ineffective. Rather, finer PSD may accelerate dissolution while the resulting dissolved products are redistributed below the sampled layer or exported through drainage pathways before accumulating as near-surface exchangeable cations. Thus, PSD effects cannot be evaluated reliably from the 0–20 cm exchangeable pool alone when system openness is high.

Several evidence gaps limit stronger boundary-resolved field interpretation. The highest-value additions are field experiments that extend integration time beyond short windows, co-report baseline and post-treatment pH with application rate and PSD in raw units, quantify water inputs and drainage, sample below the conventional 0–20 cm layer, and pair exchangeable pools with porewater, drainage-water, alkalinity, dissolved inorganic carbon, cation fluxes and inorganic-carbon measurements. Trials that explicitly test whether finer PSD reduces near-surface exchangeable detection by accelerating downward redistribution or hydrological export would be especially valuable. Expanding coverage and co-reporting in these ways would improve comparability, strengthen attribution of design variables versus context, and provide a stronger measurement basis for boundary explicit ERW CDR accounting.

5 Conclusions

Using treatment-driven exchangeable Ca–Mg responses as a shared indicator of retained near-field weathering products, we show that comparability of reported ERW outcomes is constrained first by experimental openness and sampling boundary. Retained exchangeable signals systematically weaken from incubations to pots/mesocosms to field trials, indicating that field detectability depends not only on dissolution potential, but also on whether products remain in the sampled compartment or are redistributed/exported.

This boundary dependence is central to ERW CDR interpretation. Exchangeable Ca–Mg measurements can constrain near-field retention, but they do not by themselves resolve product partitioning or whole-system carbon removal. Within the current field evidence base, application rate is the clearest design variable for retained Mg and Ca+Mg signals, whereas PSD and hydroclimate effects are boundary-dependent and should not be inferred from the 0–20 cm exchangeable pool alone. Future field studies should explicitly report sampling depth, integration window, chemical context, hydrologic openness and accounting boundary, and pair exchangeable-pool measurements with deeper soil and water-chemistry observations where CDR attribution is the objective.

Competing Interests

The authors declare no competing interests.

Data availability

The source data for this meta analysis can be found on FigShare at https://doi.org/10.6084/m9.figshare.31868998.

Acknowledgements

This work is supported by the Ministry of Education, Singapore under its MOE AcRF Tier 3 award “Climate Transformation Programme“ MOE-T32022-0006. Any opinions, findings and conclusions or recommendations expressed in this material are those of the author(s) and do not reflect the views of the Ministry of Education, Singapore.

References:

Amann, T. & Hartmann, J. (2015) On nutrients and trace metals; effects from enhanced weathering. *American Geophysical Union Fall Meeting* (2015). https://pubs-geoscienceworld-org.remotexs.ntu.edu.sg/georef/record/6/3858250/On-nutrients-and-trace-metals-effects-from

Amann, T. & Hartmann, J. (2022) Carbon accounting for enhanced weathering. *Frontiers in Climate*, 4, 849948. https://doi.org/10.3389/fclim.2022.849948

Amann, T. et al. (2020) Enhanced weathering and related element fluxes – a cropland mesocosm approach. *Biogeosciences*, 17(1), 103EP–103. https://doi.org/10.5194/bg-17-103-2020

Assink, M. & Wibbelink, C.J.M. (2016) Fitting three-level meta-analytic models in R: a step-by-step tutorial. *The Quantitative Methods for Psychology*, 12(3), 154–174. https://doi.org/10.20982/tqmp.12.3.p154

Baek, S.H.H. et al. (2023) Impact of climate on the global capacity for enhanced rock weathering on croplands. *Earth's Future*, 11(8). https://doi.org/10.1029/2023EF003698

Banwart, S.A. et al. (2019) Ground basalt application to agricultural land as an enhanced weathering strategy for CO2 sequestration. *American Geophysical Union Fall Meeting* (2019). https://pubs-geoscienceworld-org.remotexs.ntu.edu.sg/georef/record/6/4813615/Ground-basalt-application-to-agricultural-land-as

Beerling, D.J. et al. (2020) Potential for large-scale CO2 removal via enhanced rock weathering with croplands. *Nature*, 583(7815), 242–248. https://doi.org/10.1038/s41586-020-2448-9

Beerling, D.J. et al. (2024) Enhanced weathering in the US Corn Belt delivers carbon removal with agronomic benefits. *Proceedings of the National Academy of Sciences*, 121(9), e2319436121. https://doi.org/10.1073/pnas.2319436121

Beerling, D.J. et al. (2025) Challenges and opportunities in scaling enhanced weathering for carbon dioxide removal. *Nature Reviews Earth & Environment*, 6(10), 672–686. https://doi.org/10.1038/s43017-025-00713-7

Buckingham, F.L. et al. (2022) Soil core study indicates limited CO2 removal by enhanced weathering in dry croplands in the UK. *Applied Geochemistry*, 147, 105482. https://doi.org/10.1016/j.apgeochem.2022.105482

Cipolla, G. et al. (2021) The role of hydrology on enhanced weathering for carbon sequestration II. From hydroclimatic scenarios to carbon-sequestration efficiencies. *Advances in Water Resources*, 154, 103949. https://doi.org/10.1016/j.advwatres.2021.103949

Cipolla, G. et al. (2022) Effects of precipitation seasonality, irrigation, vegetation cycle and soil type on enhanced weathering – modeling of cropland case studies across four sites. *Biogeosciences*, 19(16), 3877–3896. https://doi.org/10.5194/bg-19-3877-2022

Dietzen, C., Harrison, R. & Michelsen-Correa, S. (2018) Effectiveness of enhanced mineral weathering as a carbon sequestration tool and alternative to agricultural lime: an incubation experiment. *International Journal of Greenhouse Gas Control*, 74, 251–258.

Dietzen, C. & Rosing, M.T. (2023) Quantification of CO2 uptake by enhanced weathering of silicate minerals applied to acidic soils. *International Journal of Greenhouse Gas Control*, 125, 103872. https://doi.org/10.1016/j.ijggc.2023.103872

Epihov, D.Z. et al. (2024) Iron chelation in soil: scalable biotechnology for accelerating carbon dioxide removal by enhanced rock weathering. *Environmental Science & Technology*, 58(27), 11970–11987. https://doi.org/10.1021/acs.est.3c10146

Goll, D.S. et al. (2021) Potential CO2 removal from enhanced weathering by ecosystem responses to powdered rock. *Nature Geoscience*, 14(8), 545–549. https://doi.org/10.1038/s41561-021-00798-x

Goren, A.Y., Erdemir, D. & Dincer, I. (2024) Comprehensive review and assessment of carbon capturing methods and technologies: an environmental research. *Environmental Research*, 240, 117503. https://doi.org/10.1016/j.envres.2023.117503

Guo, F. et al. (2023a) Crop productivity and soil inorganic carbon change mediated by enhanced rock weathering in farmland: a comparative field analysis of multi-agroclimatic regions in central China. *Agricultural Systems*, 210, 103691. https://doi.org/10.1016/j.agsy.2023.103691

Guo, F. et al. (2023b) Improving food security and farmland carbon sequestration in China through enhanced rock weathering: field evidence and potential assessment in different humid regions. *Science of The Total Environment*, 903, 166118. https://doi.org/10.1016/j.scitotenv.2023.166118

695 Gusenbauer, M., and Haddaway, N.R. (2020) Which academic search systems are suitable for
696 systematic reviews or meta-analyses? Research Synthesis Methods, 11, 181–217.
697 https://doi.org/10.1002/jrsm.1378

698 Haque, F. et al. (2019) Co-benefits of wollastonite weathering in agriculture: CO2 sequestration
699 and promoted plant growth. *ACS Omega*, 4(1), 1425–1433.
700 https://doi.org/10.1021/acsomega.8b02477

701 Haque, F. et al. (2023) Constraining the capacity of global croplands to CO2 drawdown via
702 mineral weathering. *ACS Earth and Space Chemistry*, 7(7), 1294–1305.
703 https://doi.org/10.1021/acsearthspacechem.2c00374

704 Hartmann, J. et al. (2013) Enhanced chemical weathering as a geoengineering strategy to
705 reduce atmospheric carbon dioxide, supply nutrients, and mitigate ocean acidification. *Reviews*
706 *of Geophysics*, 51(2), 113–149. https://doi.org/10.1002/rog.20004

707 Hasemer, H., Borevitz, J. & Buss, W. (2024) Measuring enhanced weathering: inorganic
708 carbon-based approaches may be required to complement cation-based approaches. *Frontiers*
709 *in Climate*, 6, 1352825. https://doi.org/10.3389/fclim.2024.1352825

710 Holden, F.J. et al. (2024) In-field carbon dioxide removal via weathering of crushed basalt
711 applied to acidic tropical agricultural soil. *Science of The Total Environment*, 955, 176568.
712 https://doi.org/10.1016/j.scitotenv.2024.176568

713 Holzer, I.O., Nocco, M.A. & Houlton, B.Z. (2023) Direct evidence for atmospheric carbon
714 dioxide removal via enhanced weathering in cropland soil. *Environmental Research*
715 *Communications*, 5(10), 101004. https://doi.org/10.1088/2515-7620/acfd89

716 Khalidy, R., Chiang, Y.W. & Santos, R.M. (2023) Fate and migration of enhanced rock
717 weathering products through soil horizons; implications of irrigation and percolation regimes.
718 *CATENA*, 233, 107524. https://doi.org/10.1016/j.catena.2023.107524

719 Lajeunesse, M.J. (2015) Bias and correction for the log response ratio in ecological meta-
720 analysis. *Ecology*, 96, 2056–2063. https://doi.org/10.1890/14-2402.1

721 Larkin, C.S. et al. (2022) Quantification of CO2 removal in a large-scale enhanced weathering
722 field trial on an oil palm plantation in Sabah, Malaysia. *Frontiers in Climate*, 4, 959229.
723 https://doi.org/10.3389/fclim.2022.959229

Levy, C.R. et al. (2024) Enhanced rock weathering for carbon removal—monitoring, reporting, and verification and environmental impacts. *Environmental Science & Technology* (2024). https://doi.org/10.1021/acs.est.4c02368

Lewis, A.L. et al. (2021) Effects of mineralogy, chemistry and physical properties of basalts on carbon capture potential and plant-nutrient element release via enhanced weathering. *Applied Geochemistry*, 132, 105023. https://doi.org/10.1016/j.apgeochem.2021.105023

Page, M.J. et al. (2021) The PRISMA 2020 statement: an updated guideline for reporting systematic reviews. *BMJ*, 372, n71. https://doi.org/10.1136/bmj.n71

Pogge Von Strandmann, P.A.E. et al. (2022) The dissolution of olivine added to soil at 4°C: implications for enhanced weathering in cold regions. *Frontiers in Climate*, 4, 827698. https://doi.org/10.3389/fclim.2022.827698

Reershemius, T. et al. (2023) Initial validation of a soil-based mass-balance approach for empirical monitoring of enhanced rock weathering rates. *Environmental Science & Technology*, 57(48), 19497–19507. https://doi.org/10.1021/acs.est.3c03609

Rinder, T. & von Hagke, C. (2021) The influence of particle size on the potential of enhanced basalt weathering for carbon dioxide removal – insights from a regional assessment. *Journal of Cleaner Production*, 315, 128178. https://doi.org/10.1016/j.jclepro.2021.128178

Sohng, J. et al. (2025) Combining organic amendments with enhanced rock weathering shifts soil carbon storage in croplands. *Science of The Total Environment*, 998, 180179. https://doi.org/10.1016/j.scitotenv.2025.180179

Strefler, J. et al. (2018) Potential and costs of carbon dioxide removal by enhanced weathering of rocks. *Environmental Research Letters*, 13(3). https://doi.org/10.1088/1748-9326/aaa9c4

Stubbs, A.R. et al. (2023) Impact of wet-dry cycles on enhanced rock weathering of brucite, wollastonite, serpentinite and kimberlite: implications for carbon verification. *Chemical Geology*, 637, 121674. https://doi.org/10.1016/j.chemgeo.2023.121674

Swoboda, P., Döring, T.F. & Hamer, M. (2022) Remineralizing soils? The agricultural usage of silicate rock powders: a review. *Science of The Total Environment*, 807, 150976. https://doi.org/10.1016/j.scitotenv.2021.150976

Taylor, L.L. et al. (2021) Increased carbon capture by a silicate-treated forested watershed affected by acid deposition. *Biogeosciences*, 18(1), 169–188. https://doi.org/10.5194/bg-18-169-2021

Uchibayashi, H. et al. (2025) Impact of basalt application on soil chemical properties and elemental uptake by paddy rice through enhanced rock weathering. *Soil Science and Plant Nutrition*, 1–12. https://doi.org/10.1080/00380768.2024.2448457

Van Der Bauwhede, R., Muys, B., Vancampenhout, K. & Smolders, E. (2024) Accelerated weathering of silicate rock dusts predicts the slow-release liming in soils depending on rock mineralogy, soil acidity, and test methodology. *Geoderma*, 441, 116734. https://doi.org/10.1016/j.geoderma.2023.116734

Vanderkloot, E. & Ryan, P. (2023) Quantifying the effect of grain size on weathering of basaltic powders: implications for negative emission technologies via soil carbon sequestration. *Applied Geochemistry*, 155, 105728. https://doi.org/10.1016/j.apgeochem.2023.105728

Viechtbauer, W. (2010) Conducting meta-analyses in R with the metafor package. Journal of Statistical Software, 36, 1–48. https://doi.org/10.18637/jss.v036.i03

Wang, F. et al. (2024) Wollastonite powder application increases rice yield and CO2 sequestration in a paddy field in Northeast China. *Plant and Soil*. https://doi.org/10.1007/s11104-024-06570-5

West, L.J. et al. (2023) Making mistakes in estimating the CO2 sequestration potential of UK croplands with enhanced weathering. *Applied Geochemistry*, 151, 105591. https://doi.org/10.1016/j.apgeochem.2023.105591

White, A.F. & Brantley, S.L. (2003) The effect of time on the weathering of silicate minerals: why do weathering rates differ in the laboratory and field? *Chemical Geology*, 202(3–4), 479–506. https://doi.org/10.1016/j.chemgeo.2003.03.001

Xu, T. et al. (2024) Enhanced silicate weathering accelerates forest carbon sequestration by stimulating the soil mineral carbon pump. *Global Change Biology*, 30(8), e17464. https://doi.org/10.1111/gcb.17464

Xu, T. et al. (2025) Enhanced rock weathering promotes soil organic carbon accumulation: a global meta-analysis based on experimental evidence. *Global Change Biology*, 31(9), e70483. https://doi.org/10.1111/gcb.70483

Supplementary Information

System openness governs detectable signals of enhanced rock weathering in soils: a global meta-analysis

Table S1. Databases and search strategy used for the systematic literature search (2018–2025).

Database/source	Search fields	Years	Query implementation	Notes
Web of Science (Core Collection)	Topic (title, abstract, author keywords, Keywords Plus)	2018–2025	Core ERW terms AND dissolution/cation terms (full string below); syntax adapted to platform	Results exported with full metadata; duplicates removed prior to screening
ScienceDirect	Advanced search (title, abstract, keywords where available)	2018–2025	Core ERW terms AND dissolution/cation terms (full string below); syntax adapted to platform	Results exported for screening; platform syntax adapted as needed
PubMed	Title/Abstract (where supported by platform query tags)	2018–2025	Core ERW terms AND dissolution/cation terms (full string below); syntax adapted to platform	Results exported for screening; soil/sediment ERW relevance assessed at full-text stage
Google Scholar	Keyword search (title/abstract not consistently separable)	2018–2025	Core ERW terms AND dissolution/cation terms; long strings simplified when required by query limits	Used to maximise coverage across indexing systems; screening followed PRISMA workflow (Fig. FS1)

Core Boolean search string (example):

("enhanced rock weathering" OR "accelerated weathering" OR "rock dust" OR "rock powder" OR "basalt amendment" OR basalt OR olivine OR wollastonite OR "silicate rock*" OR "silicate weathering" OR "alkalinity enhancement") AND ("mineral dissolution" OR "cation release" OR "Ca release" OR "Mg release")

Table S2. Commonly cited ERW CDR benchmark magnitudes under different accounting scopes

Benchmarks are grouped into (A) modelling/scenario estimates, (B) field-trial estimates, and (C) policy/engineering illustrative conversions. Values are not directly comparable across rows because boundaries, time horizons, and measurement compartments differ.

Panel	Reference	Context / scenario	Accounting basis (boundary)	Reported magnitude	Key notes / assumptions
A	Baek et al. (2023) Earth's Future. DOI: 10.1029/2023EF003698	Global 1-D reactive transport + climate experiments (~1,000 cropland sites). Basalt application: 10 t ha−1 yr−1; PSD: P80 = 100 μm.	Modelled area-normalised net CDR (croplands)	Global mean ~1.14–1.16 t CO2 ha−1 yr−1	Reported regional variation: North America/Europe ~1; Australia <0.6; parts of Africa/Thailand/ E China/India ~1.2–1.6 (order-of-magnitude context).
A	Beerling et al. (2025) Nature. DOI: 10.1038/s41586-024-08429-2	US state-level scenario. Annual crushed basalt: 40 t ha−1; PSD: P80 = 100 μm; mapped net annual CDR rates per hectare (2040–	Whole-system modelling of net CDR (includes emissions penalty from mining, grinding, transport, spreading).	National total: 0.16–0.30 Gt CO2 yr−1 by 2050; 0.25–0.49 Gt CO2 yr−1 by 2070	Per-hectare CDR is spatially heterogeneous (see Fig. 1c,d in source); values depend on timing of deployment, soil pH, crop type, climate, and supply constraints.

		2050; 2060–2070).			
A	Beerling et al. (2020) Nature. DOI: 10.1038/s41586-020-2448-9	Global techno-economic assessment (cropland deployment).	Global potential expressed as national/aggregate CDR targets	Average global CDR targets: 0.5–2 Gt CO2 yr−1 (2050 scale)	Targets reflect broad-scale deployment potential and assumed system boundaries; not directly comparable to compartment-based soil proxies.
B	Beerling et al. (2024) PNAS. DOI: 10.1073/pnas.2319436121	US Corn Belt replicated field trial. Basalt applied each fall for 4 years: 50 t ha−1 yr−1.	Cation loss from applied basalt used to estimate conservative cumulative CDR potential (CDRpot).	10.5 ± 3.8 t CO2 ha−1 over 4 years (cumulative); trend from ~3.8 (year 1) to ~10.5 (year 4)	Reported as conservative, time-integrated potential tied to measured Ca2+ + Mg2+ loss from applied rock under site-specific hydrology and background variability.
B	McBride et al. (2025) Frontiers in Climate. DOI: 10.3389/fclim.2025.1606574	Scotland field trial; porewater time series + water balance. High application rates: 78 and 126 t	Direct pCDR estimated from porewater chemistry (site- and time-specific).	0.33–0.53 t CO2 ha−1 after ~1.5 years (5 cm depth; 78/126 t ha−1 vs control)	Authors note this high application rates are not operationally typical; porewater-only approaches may represent a minimum over the measurement

		ha−1.			period.
B	Larkin et al. (2022) Frontiers in Climate. DOI: 10.3389/fclim.2022.959229	Sabah, Malaysia oil palm catchment-scale field trial (Oct 2018–Jul 2021).	Alkalinity export + carbonate formation framework; stream chemistry corrected for inputs.	3.8 ± 0.8 (treated) vs 3.7 ± 0.6 (control) t CO2 ha−1 over monitoring period	No clear treatment–control separation within uncertainty; authors discuss dominance of fertilizer/weathering background and detectability limits.
C	Forrest & Wentworth (2024) UK Parliament POSTnote 726 (15 Aug 2024)	Illustrative conversion for silicate rock powders under assumed dissolution fractions over ~10 years.	CO2 removed per tonne of rock per year (engineering/policy framing)	0.045 t CO2 t−1 rock yr−1 (<100 μm); 0.153 t CO2 t−1 rock yr−1 (<10 μm)	Based on an example study suggesting ~16% (<100 μm) and ~55% (<10 μm) dissolution within 10 years; intended for policy context rather than site-specific MRV.

Note: Units are reported as in the original sources. Comparability across rows is limited by differing system boundaries (e.g., soil retention vs export-inclusive), time horizons, and whether estimates include lifecycle emissions penalties.

Table S3. Setting-stratified multivariable meta-regression outputs used to support Fig. 4 (exchangeable Ca).

Notes: β are standardised coefficients from REML random-effects meta-regressions; CI denotes 95% confidence interval. Full model specifications and variable transformations are described in Methods. Panel B tests openness-dependent water sensitivity with Field as the baseline category.

Panel A. Setting-stratified multivariate coefficients

Setting	Predictor	n	β	95% CI (low)	95% CI (high)	p-value	τ^2
Field	Dose (log10)	23	0.174	0.012	0.336	0.0354	0.035
Field	Baseline soil pH	23	-0.215	-0.351	-0.079	0.00199	0.035
Field	Water input (log10)	23	-0.382	-0.967	0.202	0.199	0.035
Field	Particle size (log10)	23	-0.128	-0.493	0.238	0.494	0.035
Field	Temperature	23	-0.003	-0.036	0.030	0.852	0.035
Pot	Dose (log10)	24	0.339	-0.396	1.074	0.366	0.155
Pot	Baseline soil pH	24	0.336	-0.067	0.739	0.103	0.155
Pot	Water input (log10)	24	1.715	0.182	3.249	0.0283	0.155
Pot	Particle size (log10)	24	-1.837	-3.144	-0.529	0.0059	0.155
Pot	Temperature	24	-0.077	-0.152	-0.002	0.0434	0.155
Incubation	Dose (log10)	21	-0.306	-1.497	0.885	0.615	0.277
Incubation	Baseline soil pH	21	-0.343	-0.461	-0.225	1.1e-08	0.277
Incubation	Water input (log10)	21	-0.272	-0.811	0.267	0.323	0.277
Incubation	Particle size (log10)	21	-0.197	-0.681	0.286	0.424	0.277
Incubation	Temperature	21	0.007	-0.022	0.036	0.642	0.277

Panel B. Openness interaction model for water input (Field baseline)

Term	β	SE	z	95% CI (low)	95% CI (high)	p-value
Intercept	1.970	1.145	1.720	-0.275	4.215	0.0854
Dose (log10)	0.145	0.160	0.907	-0.168	0.458	0.365
Baseline soil pH	-0.162	0.081	-1.990	-0.321	-0.002	0.0466
Particle size (log10)	-0.057	0.161	-0.352	-0.373	0.259	0.725
Temperature	-0.001	0.015	-0.082	-0.031	0.029	0.934
Water input (log10) [Field baseline]	-0.301	0.310	-0.968	-0.909	0.308	0.333
Water input × Pot	-0.102	0.288	-0.355	-0.666	0.462	0.722
Water input × Incubation	0.717	0.313	2.291	0.104	1.331	0.022
Pot (main effect)	0.871	0.986	0.883	-1.062	2.804	0.377
Incubation (main effect)	-1.864	0.883	-2.110	-3.595	-0.133	0.0348

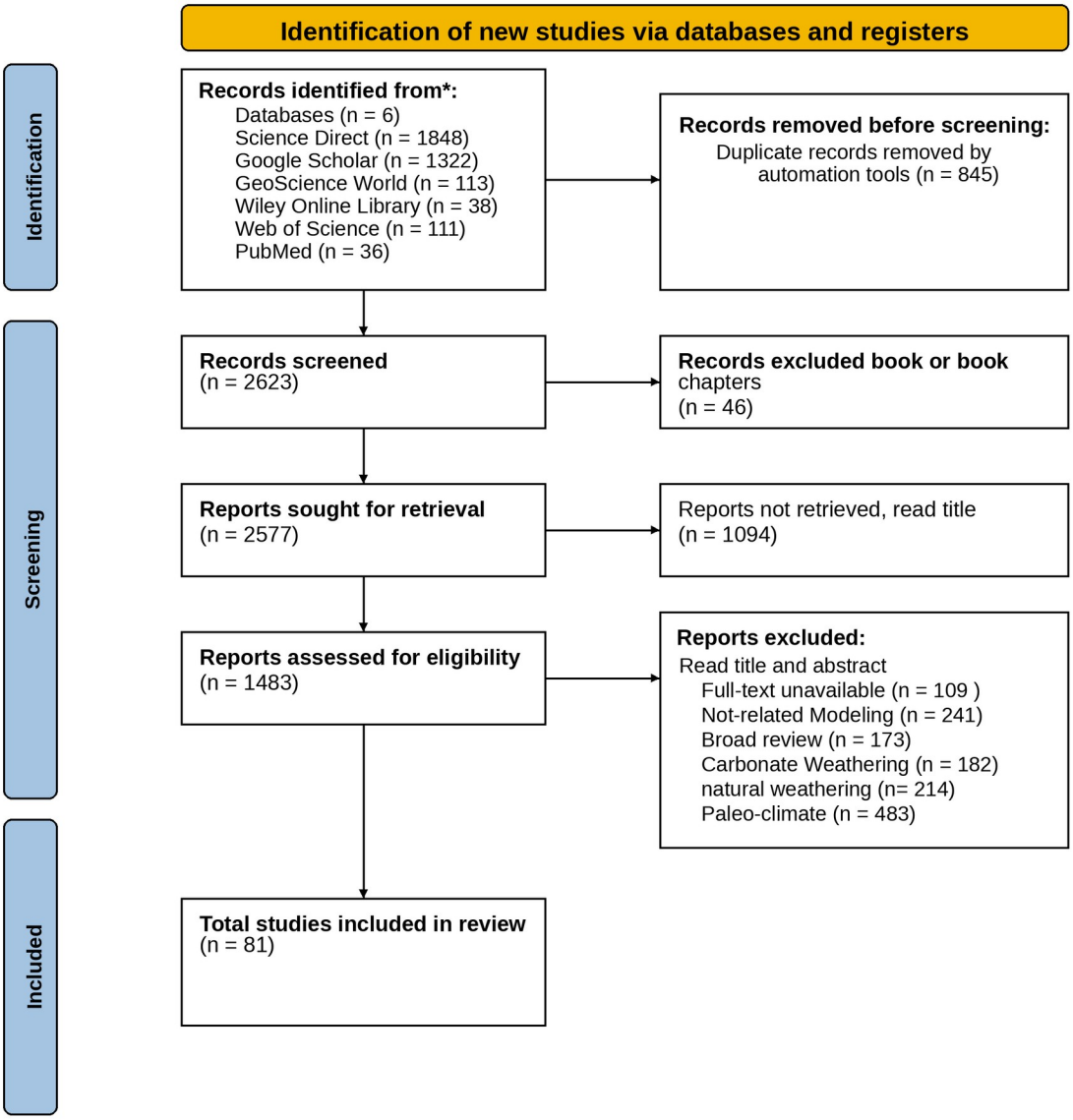

Fig. S1 PRISMA flow diagram for literature search, screening, and study inclusion of studies in the ERW meta-analysis. Boxes report numbers of records retrieved from each database, duplicates removed, records screened, full texts assessed, exclusion reasons, and the final number of studies included.

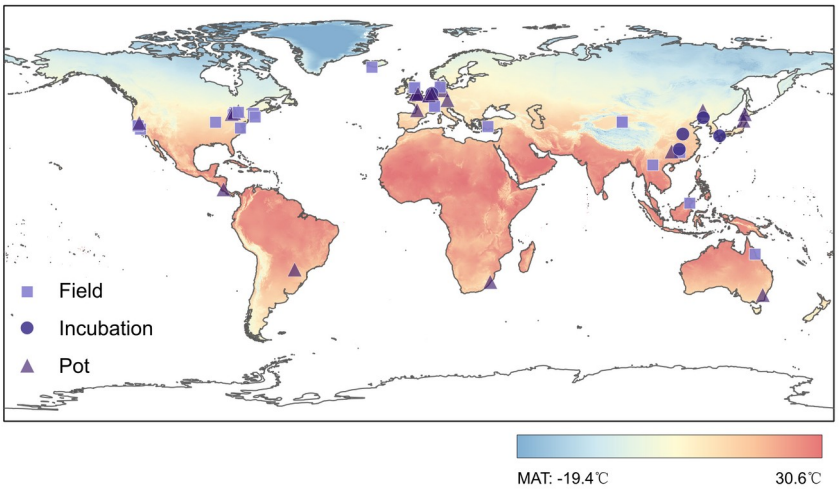

Fig.S2 Global distribution of ERW study locations across climate space. Symbols mark the geographic coordinates of studies included in the synthesis, grouped by experimental setting: field trials (squares), pot/mesocosm studies (triangles), and incubation/soil reactor experiments (circles). The background raster shows mean annual temperature (MAT, °C) from a global climatology, with the colour bar indicating the MAT range (−19.4 to 30.6 °C).

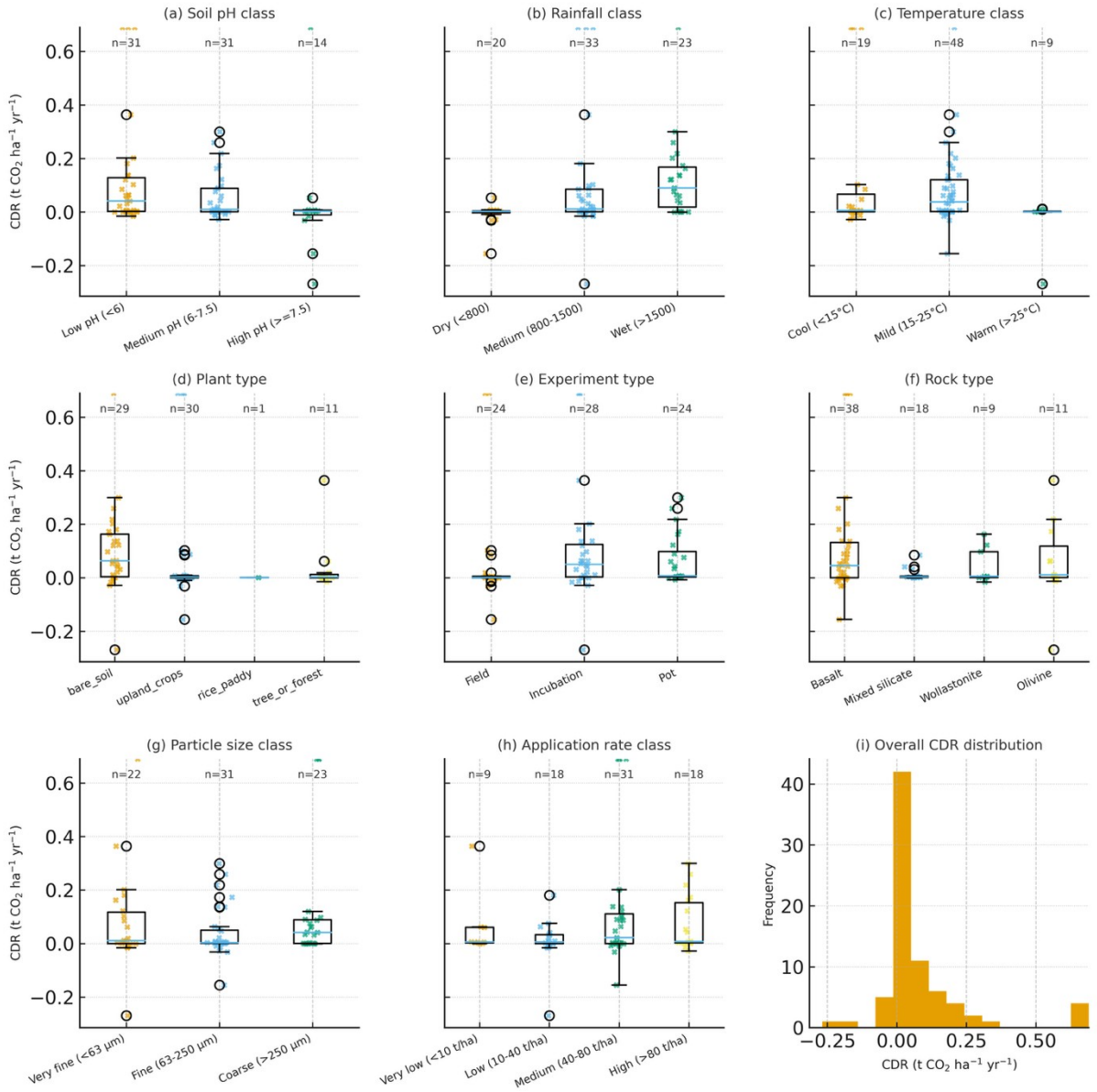

Fig. S3 Distribution of annualised converted CDR across study strata and overall. Boxplots summarise annualised converted CDR estimates (t CO_2 ha^{-1} yr^{-1}) stratified by (a) soil pH class, (b) rainfall class, (c) temperature class, (d) plant type, (e) experiment type, (f) rock type, (g) particle size class, and (h) application-rate class; points show individual comparisons and n indicates sample size per stratum. Boxes show the interquartile range with the median line; whiskers extend to 1.5×IQR and circles denote outliers. Panel (i) shows the overall frequency distribution. Positive values indicate net CO_2 removal under the adopted conversion, whereas negative values indicate zero or net-positive CO_2 flux under the same assumptions.

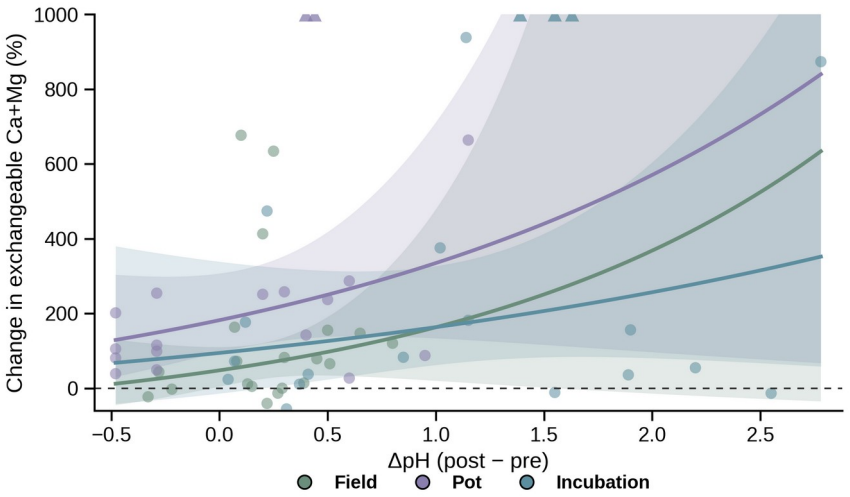

Fig. S4 | ΔpH–Ca+Mg response by setting. Scatter points show individual treatment–control contrasts (percent change in exchangeable Ca+Mg, converted from lnRR) plotted against ERW-induced pH change (ΔpH = post − pre), coloured by setting (field, pot/mesocosm, incubation). Solid curves indicate fitted setting-specific trends with 95% confidence bands. The dashed line marks no change (0%).

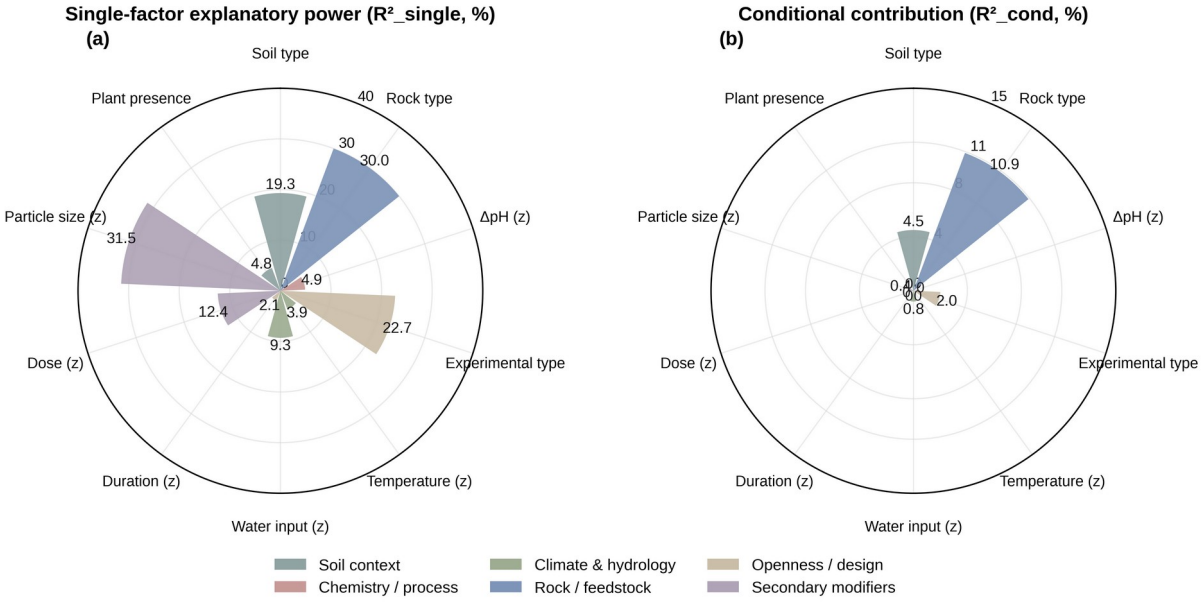

Fig. S5 | Relative importance of predictors for exchangeable Ca+Mg responses. Radar plots compare (a) single-factor explanatory power (R^2_single) and (b) conditional contribution in the multivariable model (R^2_cond) across grouped drivers (soil context, chemistry/process, climate–hydrology, rock/feedstock, openness/design and secondary modifiers). Values are expressed as percentages of variance explained.

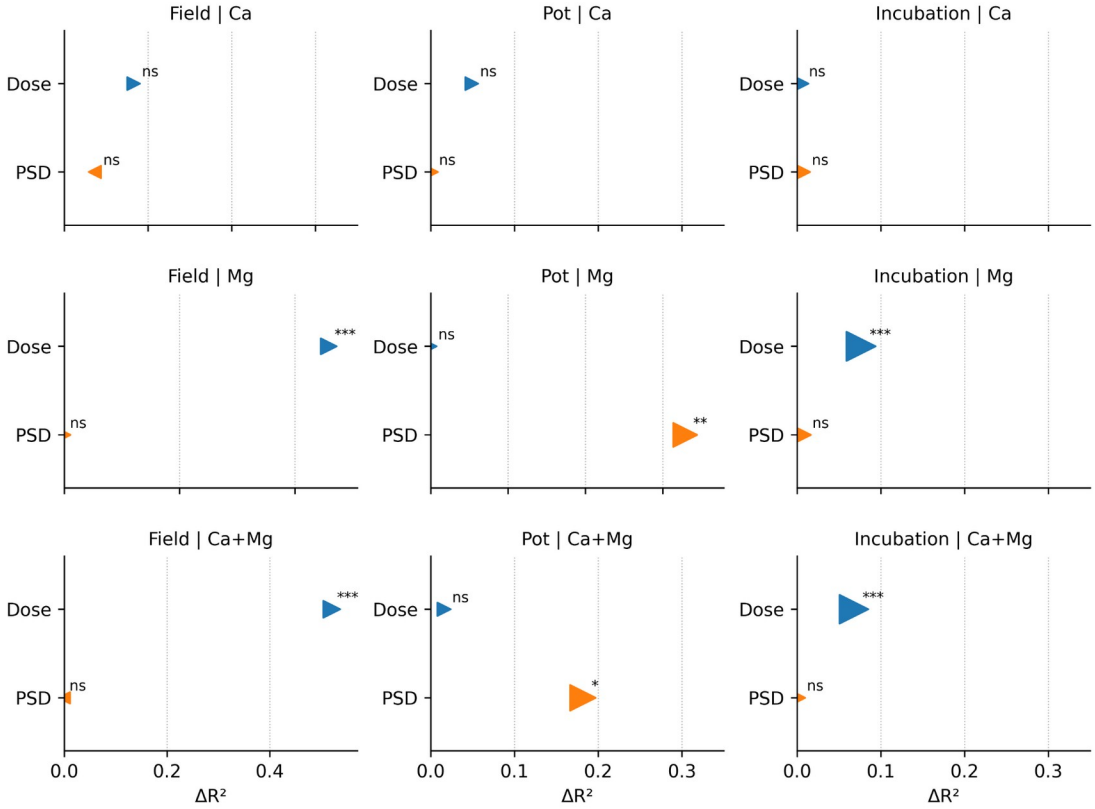

Fig. S6 | Conditional importance of controllable levers across settings and ions. Panels show the conditional contribution (ΔR^2) of application rate (Dose) and particle size distribution (PSD) to multivariable models for exchangeable Ca, Mg and Ca+Mg, stratified by field, pot/mesocosm and incubation studies. Triangles denote ΔR^2 for each predictor (larger = greater contribution). Statistical significance is indicated as ns, *P < 0.05, **P < 0.01 and ***P < 0.001.

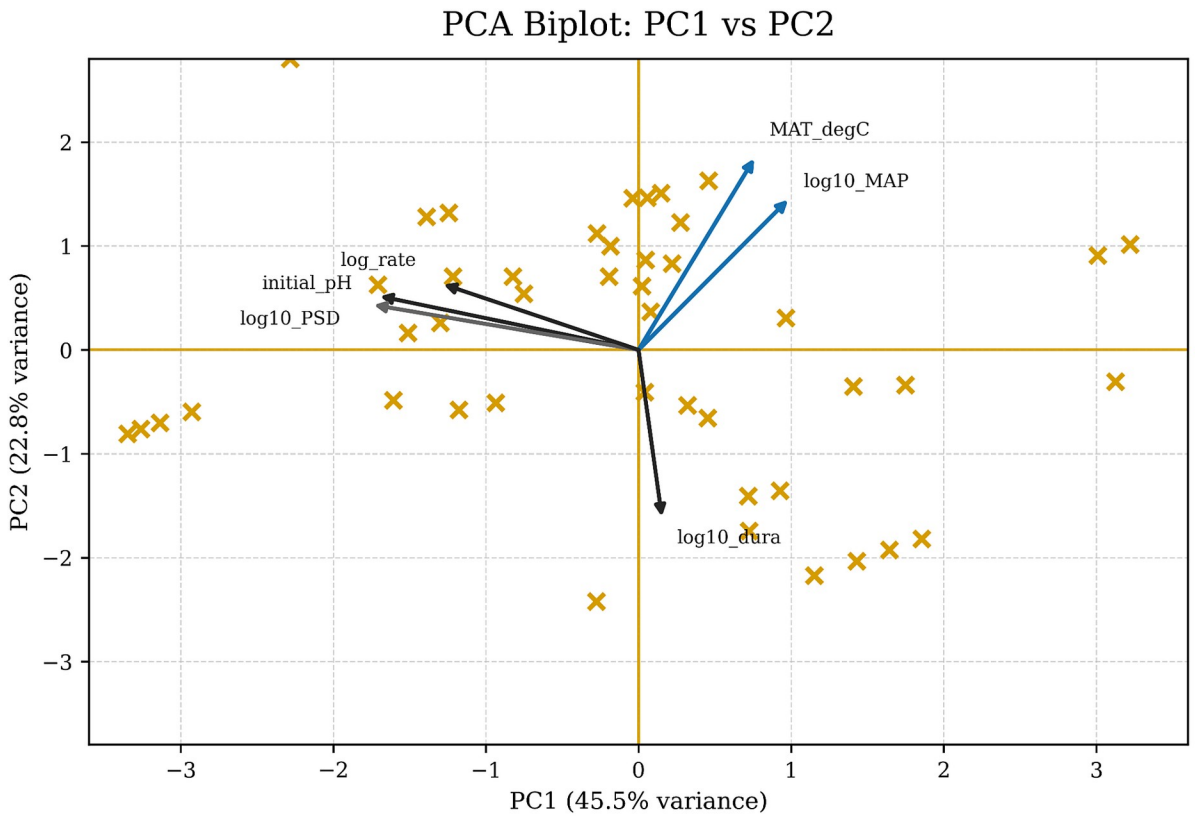

Fig. S7 PCA biplot of co-variation among reported study design and environmental variables in the ERW evidence base. Principal component analysis (PCA) biplot showing PC1 versus PC2 for the set of co-reported moderators (e.g., application rate, particle size, baseline pH, duration, MAP and MAT). Points represent individual comparisons/studies projected into the PCA space. Arrows indicate variable loadings (direction and magnitude), highlighting correlation structure and common co-occurrence patterns among deployment variables and environmental context within the compiled literature (percent variance explained shown on axes).

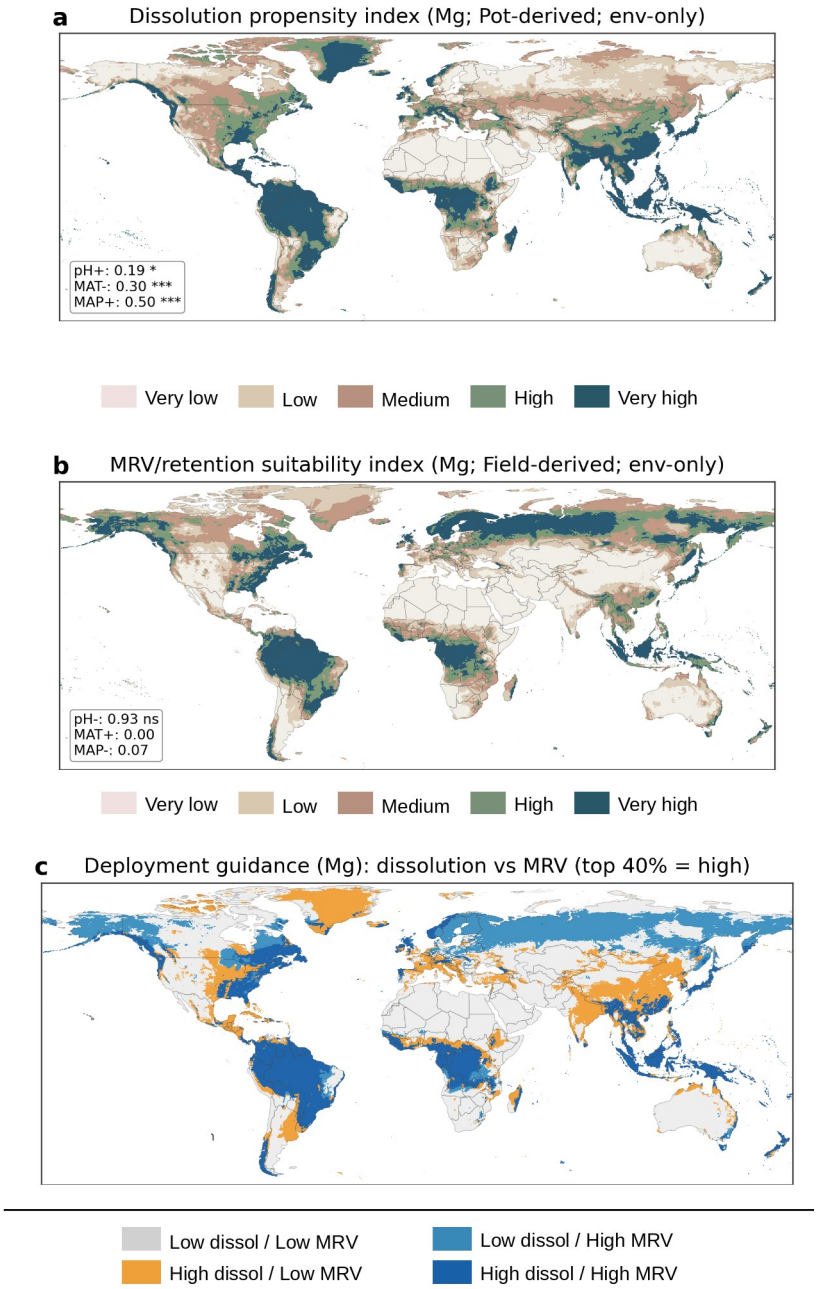

Fig. S8 Environment-only mapping for Mg responses. Global quintile maps of (a) pot-derived dissolution propensity and (b) field-derived MRV/retention suitability for Mg, estimated from SoilGrids pH (0–30 cm) and WorldClim MAT/MAP using evidence-weighted coefficients. (c) Bivariate deployment guidance classifies cells by whether each index falls in the top 40% (high) versus lower 60%.

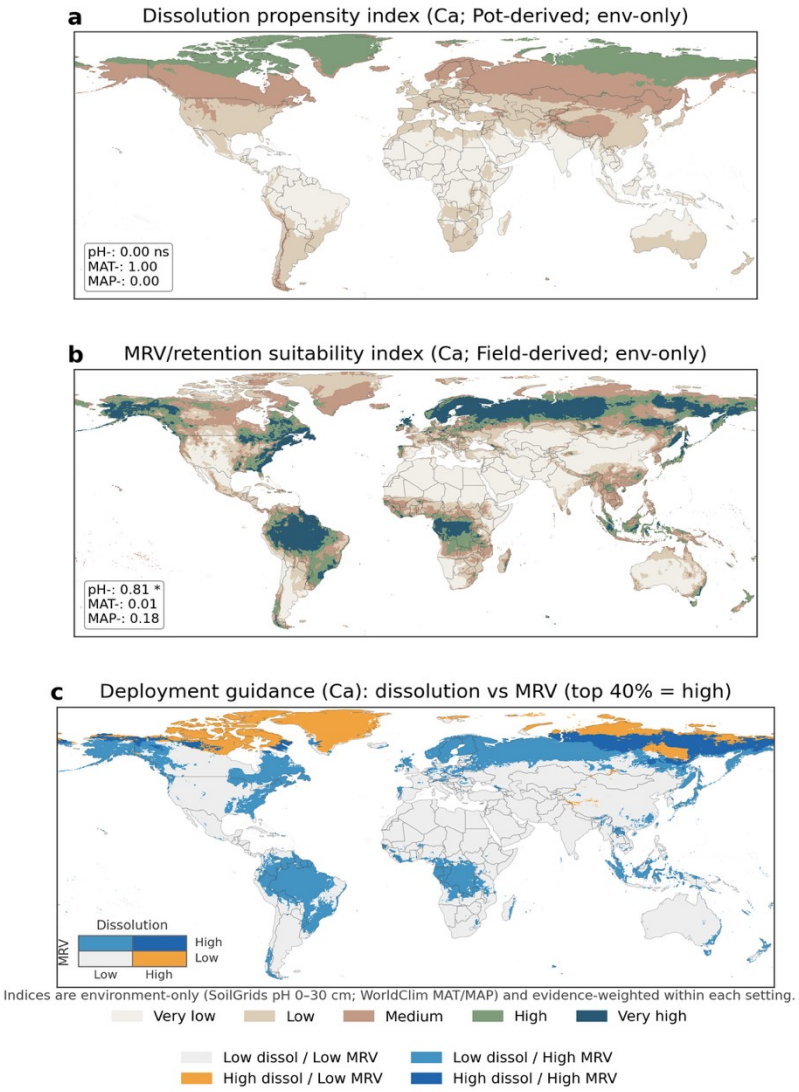

Fig. S9 Environment-only mapping for Ca responses. Global quintile maps of (a) pot-derived dissolution propensity and (b) field-derived MRV/retention suitability for Ca, estimated from SoilGrids pH (0–30 cm) and WorldClim MAT/MAP using evidence-weighted coefficients. (c) Bivariate deployment guidance classifies cells by whether each index falls in the top 40% (high) versus lower 60%.